White Rose Research Online

eprints@whiterose.ac.uk
https://eprints.whiterose.ac.uk
Universities of Leeds, Sheffield and York

Deposited via The University of Sheffield.

White Rose Research Online URL for this paper:
https://eprints.whiterose.ac.uk/id/eprint/211133/

Version: Accepted Version

Article:
Jie, Z., Zhang, Z., Susmel, L. et al. (2024) Corrosion fatigue mechanisms and evaluation methods of high-strength steel wires: a state-of-the-art review. Fatigue & Fracture of Engineering Materials & Structures, 47 (7). pp. 2287-2318. ISSN: 8756-758X

https://doi.org/10.1111/ffe.14311

© 2024 The Authors. Except as otherwise noted, this author-accepted version of a journal article published in Fatigue & Fracture of Engineering Materials & Structures is made available via the University of Sheffield Research Publications and Copyright Policy under the terms of the Creative Commons Attribution 4.0 International License (CC-BY 4.0), which permits unrestricted use, distribution and reproduction in any medium, provided the original work is properly cited. To view a copy of this licence, visit http://creativecommons.org/licenses/by/4.0/

Reuse
This article is distributed under the terms of the Creative Commons Attribution (CC BY) licence. This licence allows you to distribute, remix, tweak, and build upon the work, even commercially, as long as you credit the authors for the original work. More information and the full terms of the licence here: https://creativecommons.org/licenses/

Takedown
If you consider content in White Rose Research Online to be in breach of UK law, please notify us by emailing eprints@whiterose.ac.uk including the URL of the record and the reason for the withdrawal request.

UNIVERSITY OF LEEDS
University of Sheffield
UNIVERSITY of York

Corrosion fatigue mechanisms and evaluation methods of high-strength steel wires: A state-of-the-art review

Zhiyu Jie[1*], Zenghui Zhang[1], Luca Susmel[2], Lexin Zhang[1], Wei Lu[1]

1. Department of Civil Engineering, Ningbo University, Ningbo 315211, China;

2. Department of Civil and Structural Engineering, The University of Sheffield, Sheffield S1 3JD, UK

Abstract: Corrosion significantly degrades the fatigue performance of high-strength steel wires. This study conducts an extensive review of corrosion fatigue in corroded steel wires based on relevant literature. It outlines corrosion fatigue evolution mechanisms and discusses various test methodologies. Six distinct approaches are employed to assess corrosion fatigue life. A three-stage multiscale corrosion fatigue evolution process involves pitting formation and growth, short crack propagation, and long crack propagation. Advanced fatigue assessment methods like the Theory of Critical Distances (TCD) and the Strain Energy Density (SED) are explored for predicting the corrosion fatigue life for corroded steel wires. A model utilizes an elastoplastic corrosion fatigue damage framework to comprehensively represent the complex interactions. The physics-data-driven method has garnered increasing attention due to its requirement of fewer sample data and good robustness. Moreover, the reliability method underscores its pivotal role in guaranteeing the longevity of suspenders and cables in practical settings.

Keywords: High-strength steel wires; Corrosion fatigue mechanism; Influencing factor; Corrosion fatigue test; Life assessment method;

Corresponding author.

E-mail address:jiezhiyu_8@163.com (Z. Jie)

1. Introduction

Cable-stayed bridges are widely utilized in modern bridge construction due to their ability to span considerable distances. The cable stay, a crucial element of cable-stayed bridges, transfers loads from the main girder to the cables and subsequently to the bridge towers. The composition of a cable stay generally includes anchorages affixed to both ends, a central arrangement of high-strength galvanized steel wires, and a polyethylene (PE) sheath enveloping the outer layer of the wires. To ensure the dependable safety of cable-stayed bridges during their service life, it is imperative to maintain the proper function and secure utilization of cable stays. Inevitably, the PE sheath of the cable stay may experience cracking or damage over the course of usage. The external natural environment can cause corrosion of high-strength steel wires in the cables. Consequently, this presents a significant challenge to the degradation of load-bearing capacity and safe service of cable-stayed bridges.

A cable inspection of the Forth Road Bridge revealed an 8-10% strength loss due to corrosion [1]. The infiltration of rainwater and cyclic vehicle loads often led to severe corrosion fatigue issues in most steel wires. The combined impact of corrosion and fatigue could significantly damage cables and potentially cause the collapse of entire bridge structures, as depicted in Fig. 1. Moreover, the prevalent occurrence of severe corrosion and corrosion fatigue problems has recently necessitated replacing numerous cables or suspenders in long-span bridges [2].

Fig. 1. Corrosion fatigue of high-strength steel wires.

Corrosion fatigue, a multifaceted phenomenon, has been the subject of considerable scrutiny since its initial observation by Haigh in 1917 [3]. McAdam expanded on this concept in 1926, elucidating it further through scholarly publications [4]. Fink et al. [5] first tried to investigate the corrosion fatigue of steel wires in sodium chloride solutions. Then, Takeuchi et al. [6, 7] considered fretting corrosion fatigue of high-strength steel wires. In the past two decades, scholars have begun to pay more attention to mechanical properties, fatigue strength, and life assessment of high-strength steel wires [8-10]. Despite the efforts and progress made, researchers have yet to solve many problems related to complex corrosion fatigue failure mechanisms and more accurate evaluation methods in high-strength steel wires.

Researchers have conducted extensive investigations into the mechanisms governing corrosion fatigue crack initiation and propagation [11-13]. The deleterious effects of corrosion

extend beyond mere reduction in material mechanical properties, manifesting as surface cracks and notches that hasten fatigue damage. Concurrently, fatigue loading induces stress concentration and dislocation movement, exacerbating corrosion progression and engendering a complex corrosion fatigue process. Corrosion pits on metallic surfaces significantly impact fatigue strength due to stress concentration, as shown in Fig. 2 [14]. Corrosion fatigue behavior correlates well with pit sizes, aspect ratios, spatial distributions, local stresses, and fatigue crack growth characteristics of materials [15-17]. Fatigue cracks can originate not only from the typical locations within corrosion pits but also from distinct areas such as the mouth of shallow pits and the bottom of deep pits [18]. Notably, the pits initiating cracks are not invariably the deepest ones, challenging the conventional understanding and highlighting a more complex relationship between pit depth and crack initiation [19]. In previous analyses, the transition from pits to cracks has been examined, with pits being regarded either as sources of stress concentration or as cracks [20]. When the stress intensity factor (SIF) range of corroded steel wires reaches the threshold, steel wires enter the fatigue crack growth stage under both chemical and mechanical driving forces. This enables cracks to persistently propagate even under low stresses, leading to a decrease in the effective cross-sectional area and fracture.

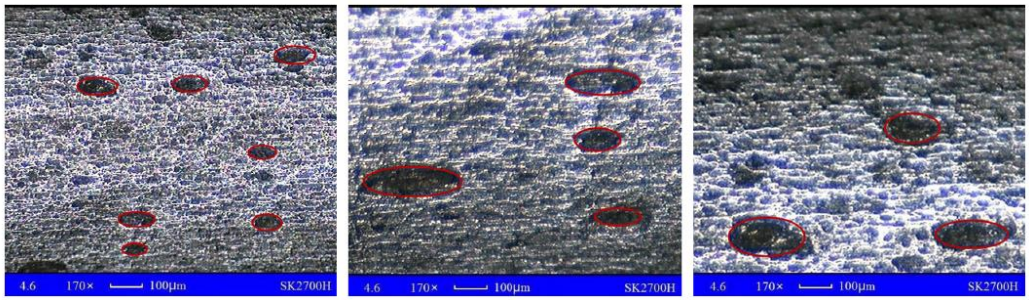

Fig. 2. Pits on a corroded steel wire surface [14].

The experimental method is applied to investigate the corrosion fatigue behavior of high-strength steel wires. These tests facilitate the exploration of intricate interactions between environmental factors and mechanical loading, thereby enhancing predictive models and refining design guidelines. The fatigue performance of high-strength steel wires in dry-wet

environments, acid-rain environments, and salt spray environments is assessed via test methods [21-23]. It is observed that fatigue strength further lowers under corrosive environments compared to dry environments. Mechanical loading conditions also significantly influence fatigue performance, with a decrease in stress ratio and/or an increase in load frequency notably prolonging corrosion fatigue life [24].

Various methods are employed to assess fatigue life, including the stress method, the energy method, the fracture mechanics method, the damage mechanics method, the data-driven method, and the reliability method. The stress method typically employs local effective stresses and S-N curves as fatigue evaluation parameters for notched components [25-27]. The energy method assesses corrosion fatigue life by considering the energy dissipated during cyclic loading, offering insights into energy-related aspects of corrosion fatigue [28, 29]. The fracture mechanics method serves as a prevalent method for the fatigue assessment of steel wires under combined cyclic loading and exposure to a corrosive medium, employing different methods to obtain initial crack sizes [30, 31]. Damage mechanics is applied for fatigue assessment by considering nonlinear damage accumulation and various initial damage scenarios [32]. Additionally, a multi-scale corrosion fatigue damage model has been developed to elucidate damage evolution during pit growth and microcrack propagation stages [33]. While the aforementioned methods establish deterministic physical models to assess fatigue life, data-driven machine learning methods have garnered considerable attention in recent years [34-36], such as Support vector machines (SVM), Gaussian process (GP), neural network (NN), random forest (RF), K-Nearest Neighbor (K-NN), and eXtreme Gradient Boosting (XGBoost), etc. To address the uncertainties stemming from load variations, environmental factors, and material properties encountered during cable service, a reliability-based method is established [37]. Probability density functions describe the distributions of corrosion pits, stress ranges, and material parameters [38, 39]. The Monte Carlo method is commonly employed to compute failure probability and the corresponding fatigue reliability index [40].

This study provides a comprehensive review of the existing literature on corrosion fatigue mechanisms and evaluation methods of high-strength steel wires (Fig. 3). A thorough

overview of corrosion fatigue evolution mechanisms is provided. Corrosion fatigue test methods are employed to determine both fatigue life prediction models and the fracture failure process. Six different life evaluation methods are elaborated upon in detail. Based on research outcomes, it is possible to make more informed decisions regarding the maintenance and replacement of high-strength steel wires in corrosive environments.

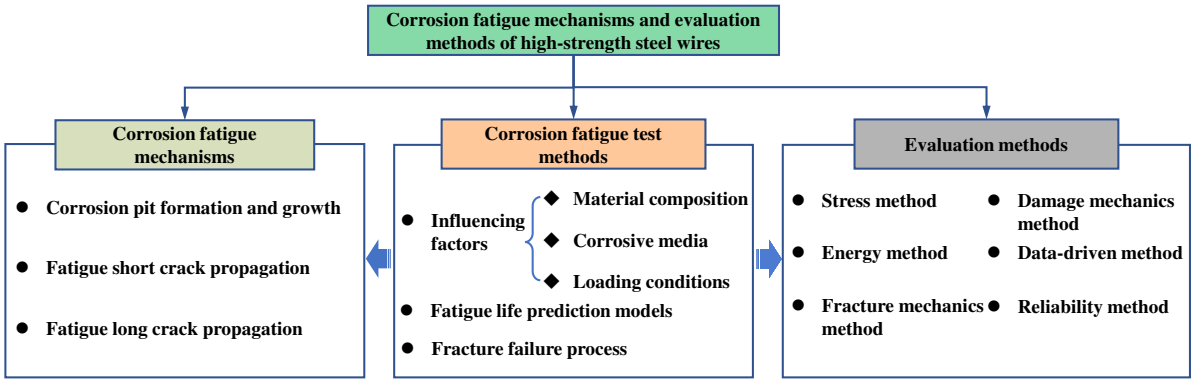

Fig. 3. Overall flowchart of this study.

2. Corrosion fatigue mechanism

2.1. Corrosion fatigue evolution process

Fig. 4 plots the corrosion fatigue evolution process for high-strength steel wires, including three distinct stages [41]. Stage 1 involves pitting formation and growth, which occur on the steel substrate of the wires. Stage 2 denotes the short crack propagation region, encompassing the transition from pitting to a short crack. This transition is influenced by the SIF threshold of the short crack. Stage 3 defines the long crack propagation phase. Throughout the corrosion fatigue process, three failure modes emerge: brittle fracture induced by pits, brittle fracture stemming from fatigue, and ductile fracture resulting from inadequate residual strength in the wire section.

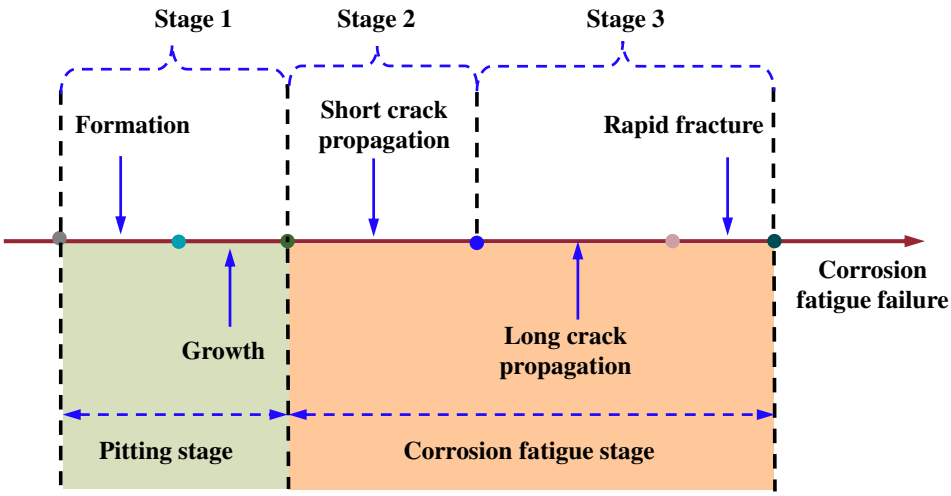

Fig. 4. Corrosion fatigue evolution process [41].

2.1.1. Pitting formation and growth

The initial stage relates to the electrochemical corrosion process of steel wires after the depletion of any zinc coating. Table 1 illustrates a comparative analysis of steel wire corrosion classification schemes sourced from different literature. Corrosion degree assessment typically relies on rust layer coloration and pit size. When metal surfaces start corroding, they often develop a thin rust layer ranging from reddish-brown to dark brown, indicating recent or mild corrosion and retaining a significant amount of their original integrity. Progressing corrosion turns the rust layer into an orange or yellowish-brown hue, suggesting increased stability but some material loss. Prolonged exposure yields a black or dark gray rust layer, signifying severe corrosion and considerable material loss, demanding attention to prevent further deterioration. Subsequently, Mild corrosion initiates shallow pits on the metal surface, which, as corrosion intensifies, can increase in both size and depth. Ref. [12] identifies four distinct pit morphologies on corroded steel wires: conical pits (i-type), hemispherical pits (ii-type), combined pits (iii-type), and secondary pits (iv-type), as depicted in Fig. 5. Varied corrosion degrees lead to different surface pit morphologies, with conical and hemispherical pits being prevalent at low corrosion degrees and combined pits and secondary pits more common at higher corrosion levels. These corrosion pits create stress concentrations on high-strength steel wire surfaces, adversely affecting the fatigue

performance. As pit depth increases and width decreases, strength diminishes gradually, accompanied by an increase in stress concentration factor (SCF). Pit clearance variation on the same side seemed to have little impact on the SCF of the steel wire. The depth of larger pits significantly affected yield strength and the SCF in steel wires with adjacent pits. Table 2 provides SCF formulas proposed by various researchers for corroded steel wires.

Table 1

Comparison of steel wire corrosion classification schemes.

NCHRP guidelines [42]		Nakamura and Suzumura [43]		Miyachi et al. [44]
Stage	Appearance	Level	Appearance	Level	Appearance
1		Initial		Initial	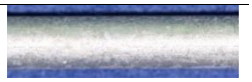
2		1		1	
3		2		2	
4		3		3	/

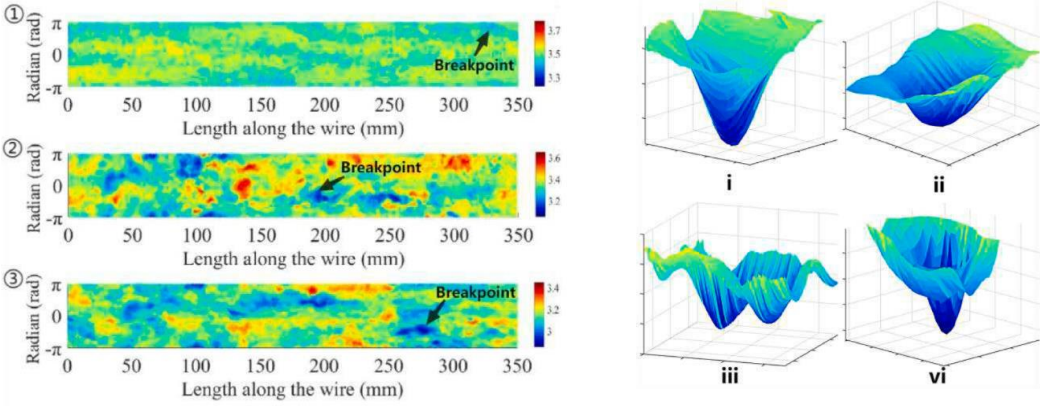

(a) (b)

Fig. 5. Corrosion morphology (a) and corrosion pits (b) [12].

Table 2

SCF calculation formulas.

Reference	SCF formula	Formula parameter
Cerit et al. [45]	$K_t = \frac{\left[1+6.6(a/2c)\right]}{\left[1+2(a/2c)\right]}$	a: pit depth $2c$: pit length

Wang et al. [46]	$K_t = \dfrac{1+3.267\left(\dfrac{d^2}{l}\right)^{0.749}}{1+1.748\left(\dfrac{d}{l^2}\right)^{0.749}}$	d: notch pit l: notch length
Jie et al. [27]	$K_t = C_1 + C_2\dfrac{d}{D} + C_3\left(\dfrac{d}{D}\right)^2 = \dfrac{1+5.4\dfrac{d}{l}}{1+1.7\dfrac{d}{l}} + \dfrac{1+862.7\dfrac{d}{l}}{1+278.2\dfrac{d}{l}} \times \dfrac{d}{D}$ $+ \dfrac{1+37.3\dfrac{d}{l}}{1-4.6\dfrac{d}{l}}\left(\dfrac{d}{D}\right)^2$	C_1, C_2, and C_3: fitting parameters d: pit radius l: pit length D: diameter of steel wire
Li et al. [47]	$K_t = A + Be^{-\left(\frac{H}{W}\right)/C} = \left[2.70984 + 8.83\times10^{-4}e^{\left(\frac{H}{T}\right)/0.06237}\right]$ $+\left[-1.7546 + 0.482e^{-76\left(\frac{H}{T}-0.22078\right)^2}\right] \times e^{-\left(\frac{H}{W}\right)/\left[\ln\left(1.92683-2.28643\times\frac{H}{T}\right)\right]}$	A, B, and C: fitting parameters H: pit depth W: pit length T: diameter of steel wire
Guo et al. [14]	$K_t = \alpha_1\left(R_{l/w}\right)^{\alpha_2} + \alpha_3\left(R_{w/d}\right)^{\alpha_4}$	α_1, α_2, α_3, and α_4: fitting parameters $R_{l/w}$: length-width ratio $R_{w/d}$: width-depth ratio

2.1.2. Crack initiation and propagation

The corrosion fatigue crack initiation mechanism is classified into four primary types [48, 49]. Firstly, the pitting acceleration theory suggests that corrosion leads to deep and localized pits on metal surfaces, causing stress concentrations and initiating cracks. Secondly, the deformation-induced anodic dissolution theory posits that electrochemical heterogeneity causes deformation in slip bands, leading to anodic regions, while non-deformed areas become cathodic. This differential activity initiates cracks due to continuous dissolution at anodic sites. Thirdly, the protective film rupture theory explains that cyclic stresses rupture the protective films formed by corrosive media on metal surfaces, creating small anodic areas. This leads to a repetitive cycle of film repair and rupture, resulting in corrosion fatigue cracks. Fourthly, the adsorption theory asserts that the adsorption of active substances from the environment onto metal surfaces reduces surface energy, causing

phenomena such as hydrogen embrittlement. In corrosion fatigue, damage manifests in two distinct forms: fatigue damage from cyclic stress and corrosive damage from environmental media. These damage types interact synergistically rather than just overlapping. The initiation mechanisms of corrosion fatigue cracks are significantly influenced by both material properties and environmental conditions. Different materials may show varied crack initiation mechanisms in the same environment, and the same material can exhibit different mechanisms under different conditions.

The phenomena of crack propagation in corrosion fatigue are inherently localized. Initiated by pitting corrosion in a corrosive environment, micro-cracks emerge from these pits and progressively propagate under cyclic loading and corrosive conditions. As crack depth increases, the influence of fatigue loading on the crack propagation rate in corrosion fatigue intensifies, ultimately becoming the predominant factor in the advanced stages of crack growth. Upon reaching a critical length, the crack expansion ceases to be governed by the electrochemical corrosion reactions within the pit. Consequently, intergranular cracks may evolve into transgranular crack propagation, precipitating rapid expansion and potentially leading to the failure of the entire specimen. The evolution from the onset of corrosion fatigue cracks at grain boundaries within corrosion pits, through the development of a primary crack, to eventual material failure, represents a gradual and intricate process. This complexity is further compounded by the involvement of corrosive media during the growth stage [50].

The process of corrosion fatigue growth can be classified into three distinct categories, based on the relationship between fatigue crack growth rate $\mathrm{d}a/\mathrm{d}N$ and SIF range ΔK, as shown in Fig. 6 [51]. Type A, which closely resembles pure fatigue, is relevant to material systems that are resistant to stress corrosion. In this category, the environment lowers the SIF threshold required for initiating crack propagation. In contrast, Type B is associated with stress corrosion fatigue and is characterized by a noticeable plateau phase. At stresses below the stress corrosion threshold, the environment does not influence crack propagation. However, as the SIF range rises, it eventually surpasses the stress corrosion threshold. At

this point, the crack growth rate experiences a sharp increase. Type C is a composite category that amalgamates features of both Types A and B. Additionally, corrosion fatigue crack propagation models are generally divided into three primary types: superposition, competitive, and product models [52]. Wei et al. [53] have developed the linear superposition model, which asserted that when the SIF exceeded the stress corrosion threshold, the corrosion fatigue crack propagation rate can be quantified as the sum of the rates of pure fatigue crack propagation and stress corrosion fatigue crack propagation. The model is mathematically represented as follows:

$$\left(\frac{\mathrm{d}a}{\mathrm{d}N}\right)_{\mathrm{CF}}=\left(\frac{\mathrm{d}a}{\mathrm{d}N}\right)_{\mathrm{F}}+\left(\frac{\mathrm{d}a}{\mathrm{d}N}\right)_{\mathrm{SCC}} \tag{1}$$

where $\left(\mathrm{d}a/\mathrm{d}N\right)_{\mathrm{CF}}$ is the corrosion fatigue crack propagation rate, $\left(\mathrm{d}a/\mathrm{d}N\right)_{\mathrm{F}}$ is the pure fatigue crack propagation rate, and $\left(\mathrm{d}a/\mathrm{d}N\right)_{\mathrm{SCC}}$ is the stress corrosion crack propagation rate. However, since Eq. (1) overlooks the influence of the interaction between corrosion and fatigue, a modified version is presented [48]:

$$\left(\frac{\mathrm{d}a}{\mathrm{d}N}\right)_{\mathrm{CF}}=\left(\frac{\mathrm{d}a}{\mathrm{d}N}\right)_{\mathrm{F}}+\left(\frac{\mathrm{d}a}{\mathrm{d}N}\right)_{\mathrm{SCC}}+\left(\frac{\mathrm{d}a}{\mathrm{d}N}\right)_{\mathrm{C}} \tag{2}$$

where $\left(\mathrm{d}a/\mathrm{d}N\right)_{\mathrm{C}}$ takes into account the interaction effects between corrosion and fatigue. Furthermore, Austen et al. [54] propose the competitive model, suggesting that the corrosion fatigue crack propagation rate results from a competition between fatigue and stress corrosion. The expression is as follows:

$$\left(\frac{\mathrm{d}a}{\mathrm{d}N}\right)_{\mathrm{CF}}=\max\left\{\left(\frac{\mathrm{d}a}{\mathrm{d}N}\right)_{\mathrm{F}},\int_{\tau}\left(\frac{\mathrm{d}a}{\mathrm{d}t}\right)_{\mathrm{SCC}}\mathrm{d}t\right\} \tag{3}$$

The product model adjusts the fatigue crack propagation rate based on empirical data. This model incorporates a correction factor D_{f} that is influenced by variables such as loading frequency f and stress ratio R. The formula is given as:

$$\left(\frac{\mathrm{d}a}{\mathrm{d}N}\right)_{\mathrm{CF}}=D_{\mathrm{f}}\left(f,R,...\right)\Delta K^{m} \tag{4}$$

where ΔK is the SIF range and *m* is a material constant.

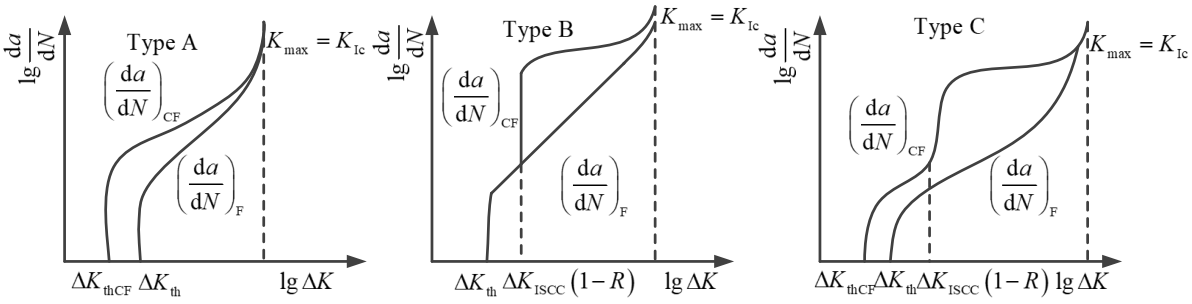

Fig. 6. Corrosion fatigue growth types [51].

2.2. Influencing factors

2.2.1. Material composition

To improve the corrosion fatigue resistance of galvanized steel wires, Galfan steel wires emerged as an innovation. These wires are produced by applying a Zn-Al alloy coating onto the steel wire surface through a hot-dip process or electroplating. Figs. 7 and 8 show the macroscopic and microscopic corrosion features of Galfan steel wires at different corrosion stages [55, 56]. The corrosion behavior of the two steel wire types exhibits exponential growth patterns. While the corrosion coefficient for galvanized steel wire follows a normal distribution, the corrosion coefficient for Galfan steel wire conforms to a Cauchy distribution. Additionally, the distribution of the maximum pitting coefficient for both galvanized and Galfan steel wire types follows a generalized extreme value distribution. It is observed that the macroscopic corrosion feature of Galfan coating progresses through four stages, while the microscopic corrosion feature unfolds across three stages. Furthermore, hot-dip Zn-Al-Mg alloy coatings have developed to prolong the stress corrosion fracture time of steel wire substrates. However, the coating type has minimal effect on the fracture morphology of steel wires [57].

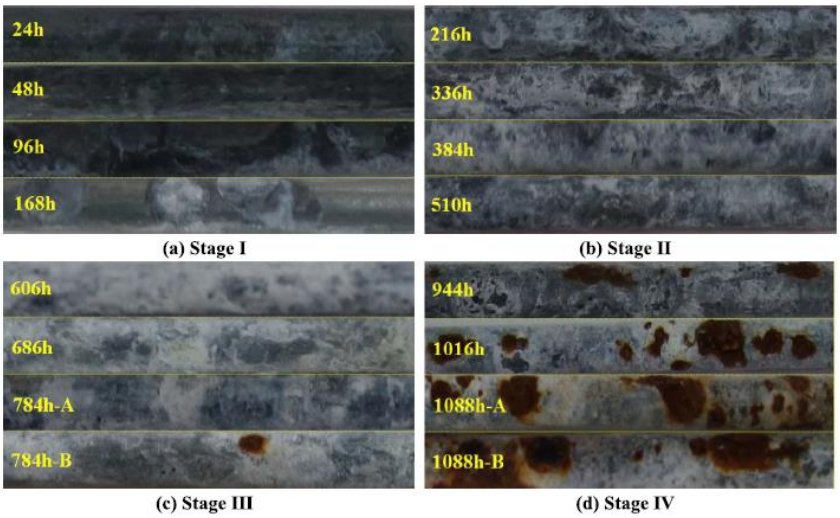

Fig. 7. Macroscopic corrosion feature analysis [57].

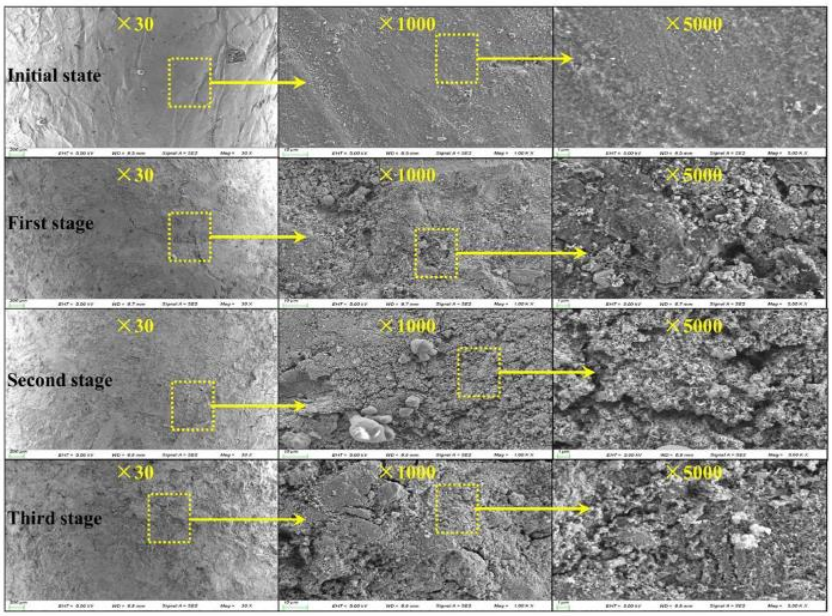

Fig. 8. Microscopic corrosion feature analysis [58].

2.2.2. Corrosive media

Fig. 9 shows the influence of relative humidity, temperature, and sodium chloride on the corrosion rate of galvanized steel wires [58]. Galvanized steel wires exhibit corrosion-free behavior at relative humidity levels below 60%. However, higher humidity levels result in increased corrosion tendencies. Moreover, as both temperature and corrosion time increase, the corrosion rate shows a corresponding increase. Beyond a relative humidity of 60%, the concentration of sodium chloride emerges as a more impactful factor on the corrosion rate.

Stress corrosion cracking incidence notably correlates with stress levels and pH, with the presence of sulfide proving more critical than its concentration [59]. Considering the impact of pH and the concentration of corrosive solutions, the logarithmic S-N curves and linear correlation coefficients for specimens in groups A-E can be determined as follows [60]:

$$\begin{aligned}
&\text{Group A}: \lg N = 14.18 - 3.741 \lg \Delta\sigma \\
&\text{Group B}: \lg N = 14.08 - 3.732 \lg \Delta\sigma \\
&\text{Group C}: \lg N = 15.00 - 4.115 \lg \Delta\sigma \\
&\text{Group D}: \lg N = 14.78 - 4.005 \lg \Delta\sigma \\
&\text{Group E}: \lg N = 15.52 - 4.347 \lg \Delta\sigma
\end{aligned} \tag{5}$$

where N is the fatigue life and $\Delta\sigma$ is the stress range. It is found that corrosion substantially reduces the lifespan of steel wires. Acidic solutions have a more pronounced adverse effect on the lifetime compared to neutral solutions, while an increase in concentration surprisingly extends the lifetime. Analyzing the impact of temperature, chloride concentration, and pH on corrosion rates using the response surface method reveals their order of effect as follows: pH, temperature, and chloride concentration [61]. Wang et al. [62] discussed the effects of loading conditions and corrosion solutions on the corrosion fatigue behavior of smooth steel wires. The corrosion fatigue behavior of steel wires at different media is seen to be significantly different. The relationships of corrosion fatigue life of steel wires in these solutions are obtained through experimental data fitting, as detailed below:

$$\text{Acid solution: } \lg N = 12.310 - 2.889 \lg \Delta\sigma \tag{6}$$

$$\text{Neutral solution: } \lg N = 11.153 - 2.416 \lg \Delta\sigma \tag{7}$$

$$\text{Alkaline solution: } \lg N = 10.348 - 2.143 \lg \Delta\sigma \tag{8}$$

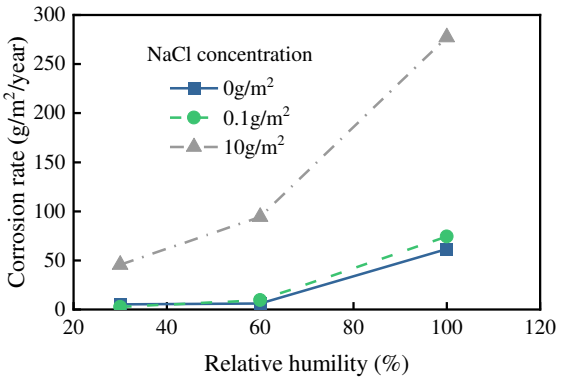

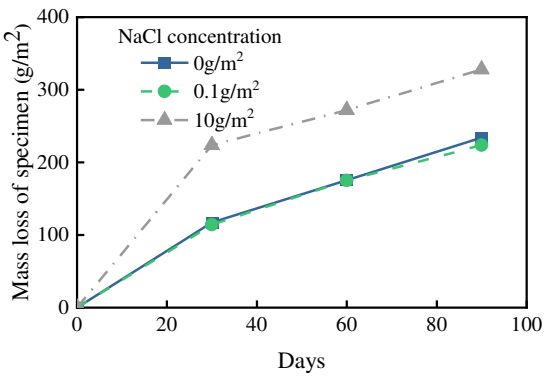

(a) (b)

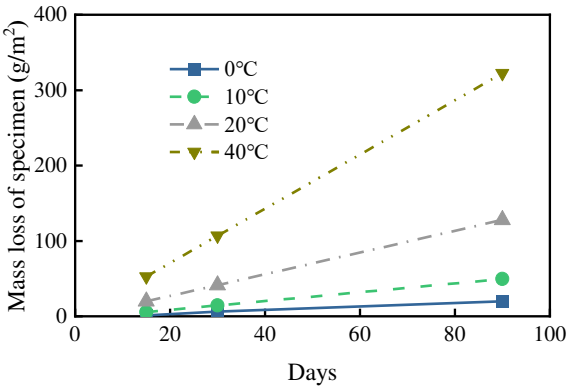

(c)

Fig. 9. Corrosion rates considering (a) relative humidity, (b) temperature, and (c) sodium chloride [58].

2.2.3. Loading conditions

Jiang et al. [24] investigated the influence of load ratios and frequencies on corrosion fatigue behavior using pre-split high-strength galvanized steel wires, as shown in Fig. 10. It reveals that lower load ratios corresponds to longer fatigue life; however, this effect is seen to diminish at lower stress amplitudes. Moreover, the impact of load frequencies on endurance life surpasses that of stress ratios. Zhang et al. [63] indicate that higher pre-stress levels correlate with increased corrosion rates in stay cable high-strength steel wires, intensifying the corrosion probability. Jie et al. [64] conducted a comprehensive study examining corroded steel wires under axial tensile fatigue loading at various stress ratios. Their regression analysis of S-N curves displayed a significant inverse correlation between corrosion fatigue life and stress ratio. Yao et al. [65] utilized accelerated salt spray corrosion tests to simulate corrosion behaviors in steel strands. Based on their experimental results, it was seen that noting changes in corrosion degrees under alternating loads and chloride environments. Additionally, Yu [66] emphasizes that environmental factors primarily influence the fatigue life of steel wires, especially at low-stress amplitudes. In cases of mild corrosion, cracks typically initiate from singular pit defects. However, as corrosion intensifies, pit depths increase, leading to cracks originating from various fatigue sources.

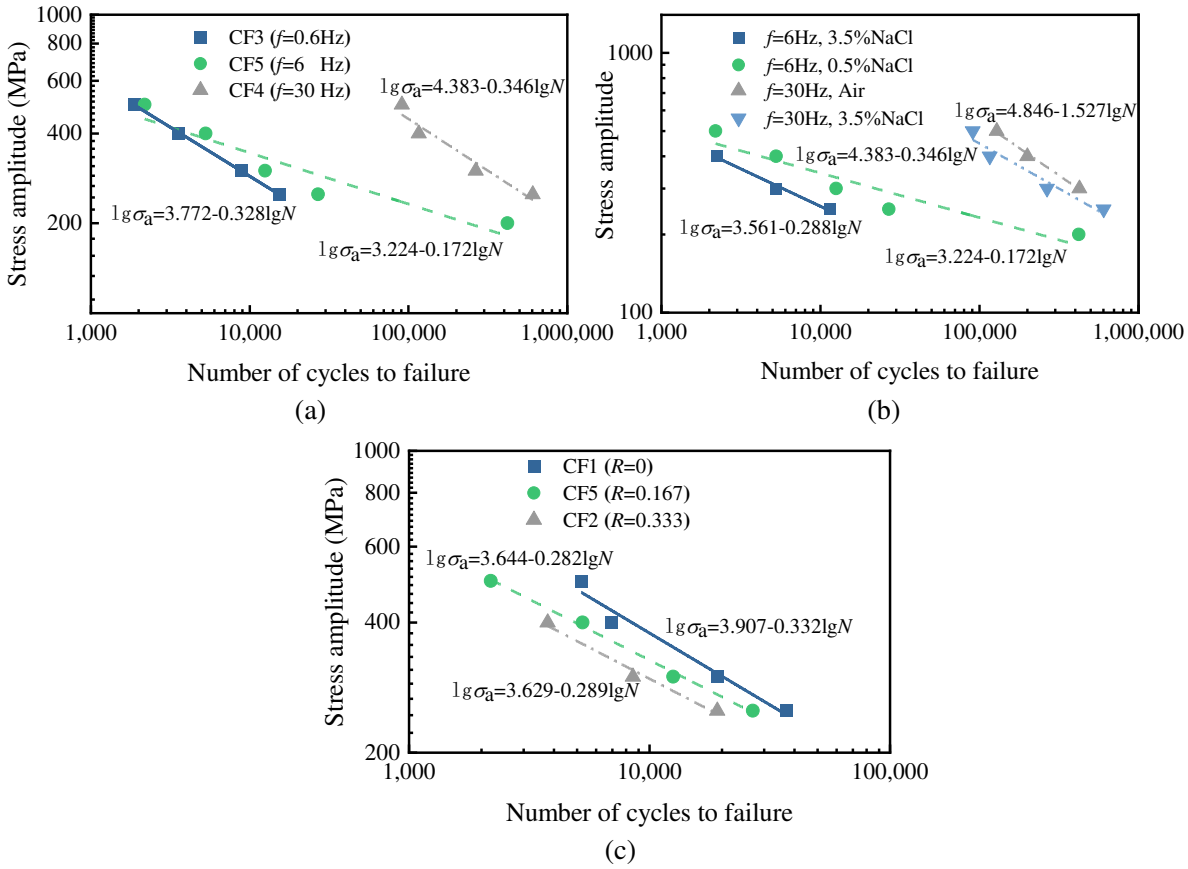

Fig. 10. Effect of load frequency (a), corrosion media (b), and load ratio (c) on the corrosion fatigue life [24].

3. Corrosion fatigue test methods

To characterize the coupling effects of corrosion and fatigue in steel wires, a novel corrosion fatigue device is developed, as illustrated in Fig. 11 [22]. This innovative assembly, integrating electrochemical accelerated corrosion elements within a tank, pumps, electrodes, and a fatigue testing machine, facilitated synchronized corrosion and fatigue testing. According to the Chinese standard of GB/T 10125 [67], the wire underwent immersion in a controlled 3.5% NaCl solution, maintaining stable temperature and oxygen levels while subjected to cyclic fatigue loads. In a study by Ma et al. [68], fatigue crack growth (FCG) tests were performed on steel wires featuring a 0.5mm depth and 0.15mm width notch within corrosive environments. Employing a servo-hydraulic universal testing machine MTS (Fig. 12), a rubber hose containing a 5% NaCl glacial acetic acid solution is attached to the steel

wire. The study applied a two-stage fatigue loading method, varying stress ranges and stress ratios on steel wire specimens, resulting in distinct fatigue fracture features.

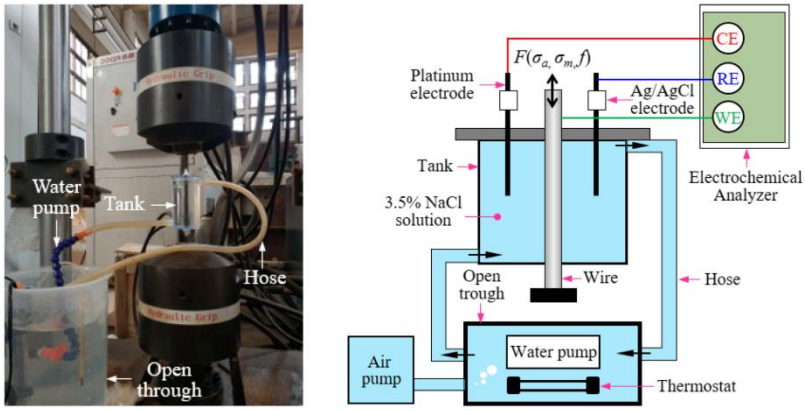

Fig. 11. Corrosion fatigue loading setup [22].

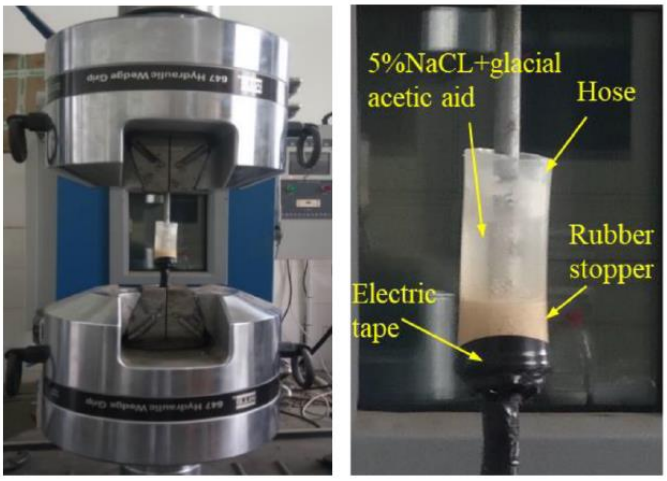

Fig. 12. MTS machine and corrosion setup [68].

Fig. 13 shows four different fracture types observed in uncorroded and corroded steel wires: cup-and-cone fracture, milling-cutter fracture, cleavage-milling-cutter fracture, and cleavage fracture [23]. Necking, indicating ductile fractures, is visible in cup-and-cone and milling-cutter specimens, contrasting the absence of necking in cleavage and cleavage-milling-cutter fractures due to reduced ductility and increased brittleness. Fig. 14 shows the corrosion fatigue fracture morphology of wires [22]. The fracture surface delineates various regions, including smooth crack propagation areas, a central ductile fracture region marked with radial patterns, and peripheral brittle fracture regions, primarily concentrated at the weakest anti-shear sections. The presence of multiple corrosion pits plays a pivotal role in

initiating stochastic cracks, resulting in intricate fracture morphologies characterized by two or three crack propagation subregions, showcasing the complexity of corrosion-induced fatigue. The impact of multiple pits is particularly notable when pit depths are relatively shallow, significantly influencing fatigue life. Guo et al. [69] delved into fracture morphology to understand the influence of load conditions and environmental aggressiveness on FCG behavior in accordance with the ASTM standard E647 [70] (Figs. 15 and 16). Examination of fracture morphologies at varying load ratios (R=0.1 and R=0.5) and crack lengths revealed that larger tear-formed ridges were associated with superior material resistance, with R=0.1 displaying larger ridges. Accelerated corrosion resulted in diminished ridges and increased corrosion facets, indicating heightened material susceptibility to fracture in more aggressive environments. Furthermore, the presence of intergranular secondary cracks and reduced ductility at higher stress ratios highlighted the detrimental impact of increased aggressiveness on material behavior in corrosive settings.

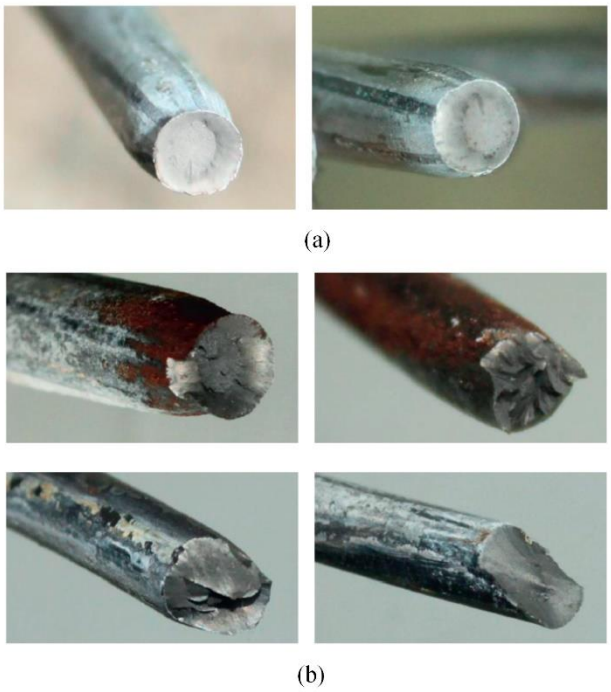

Fig. 13. Fracture types of uncorroded (a) and corroded (b) steel wires [23].

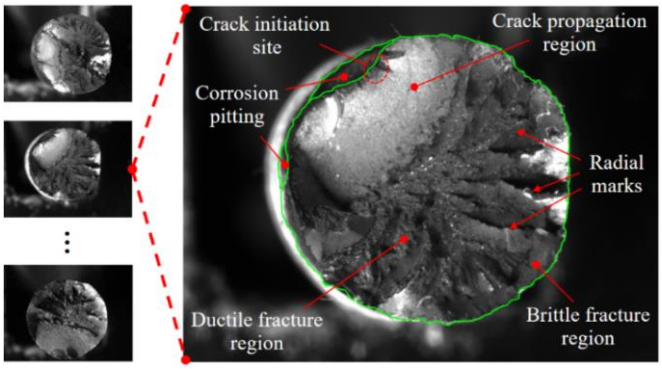

Fig. 14. Corrosion fatigue fracture morphology [22].

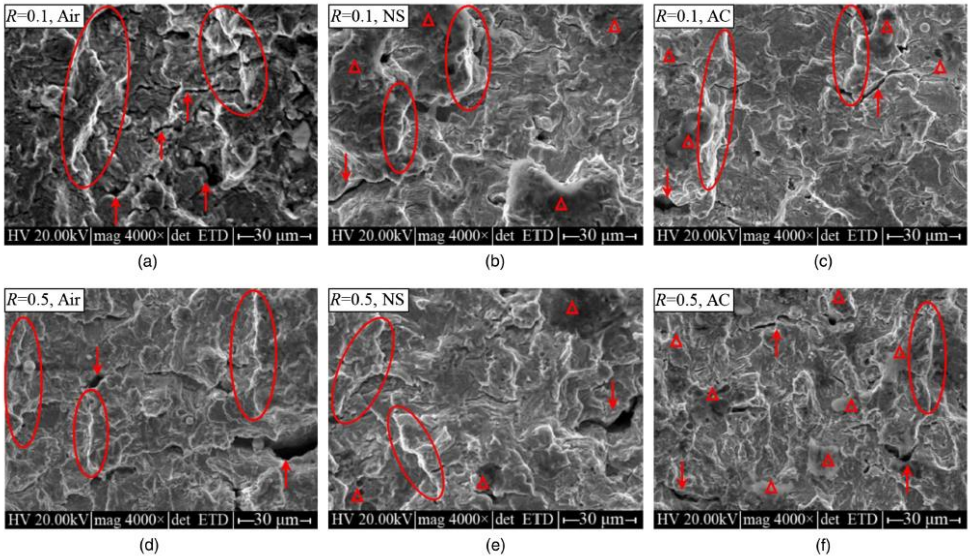

Fig. 15. SEM images of fracture morphology in stable crack growth region [69].

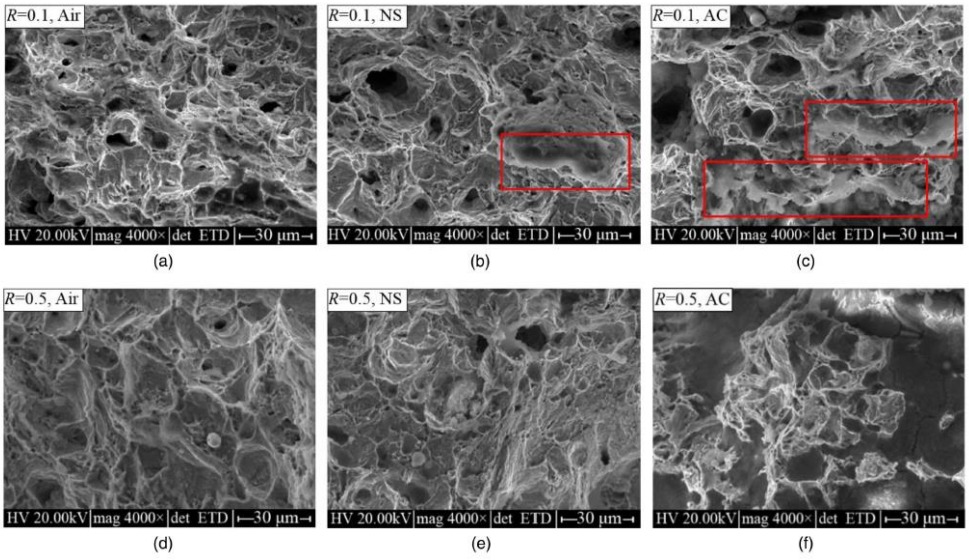

Fig. 16. SEM images of fracture morphology in unstable crack growth region [69].

Fig. 17 shows the fatigue testing equipment and a specially designed clamp tailored for corroded high-strength steel strands [71]. In Fig. 18, the curves depicting fatigue life concerning corrosion time and rate for high-strength steel strands are presented, with the corresponding fitting formulas derived through the least squares method being expressed as:

$$N = 67854.838 + 104547.976 \times 0.74^{t} \quad (9)$$

$$N = -70321.12 + 216366.4 \times 0.947^{\eta} \quad (10)$$

The fatigue life exhibits a declining trend as the service time increases. Initially, when the steel strand has a service life of fewer than 8 years, the fatigue life exceeds 100,000 cycles. Subsequently, as the steel strand ages within the 8 to 13-year service range, the fatigue life consistently falls within the range of 50,000 to 80,000 cycles.

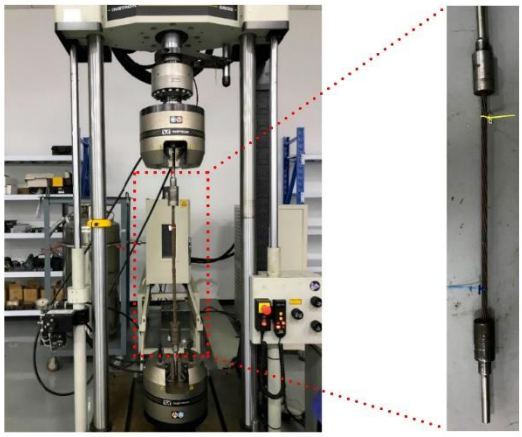

Fig. 17. Fatigue testing equipment for corroded high-strength steel strands [71].

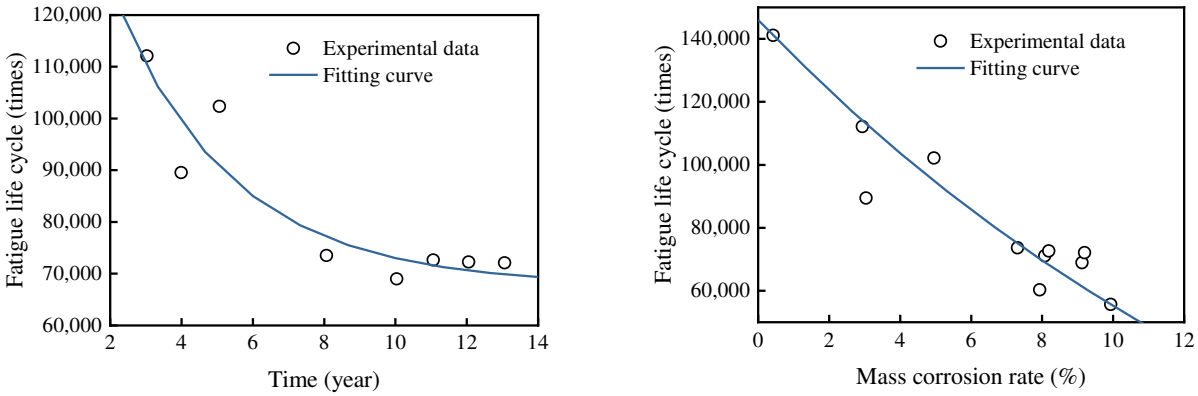

Fig. 18. Fatigue lives versus corrosion time (a) and corrosion rate (b) [71].

In summary, the coupling effects of corrosion and fatigue in steel wires were rigorously

investigated through innovative testing setups integrating electrochemical corrosion elements with fatigue testing machines. The outcomes from these studies reveal distinct fracture types influenced by corrosive environments, showcasing ductile features in uncorroded specimens versus brittle fractures in corroded wires. Fractography of corroded wires highlights the role of corrosion pits in initiating complex crack propagation, affecting fatigue life significantly. Additionally, examination of fracture morphology under varying load conditions and environmental aggressiveness emphasizes the detrimental impact of increased corrosion on material behavior, leading to reduced fatigue resistance.

4. Corrosion fatigue assessment methods

4.1. Stress method

The stress method, including both nominal and local stresses, serves as a prevalent means to evaluate the fatigue characteristics of corroded steel wires. It delves into the impact of steel wire type, corrosion degree, pit shape and size, stress range, and stress ratio on the fatigue life. Fig. 19 displays S-N curves for different steel wire types under different corrosion degrees, revealing the superior corrosion fatigue resistance of Zn-Al alloy-coated steel wire over Zn-coated counterparts [72]. Notably, as the corrosion degree increases, the S-N curve steepens, precipitating a swifter decline in fatigue life, particularly evident at lower stress ranges. Moreover, high stress ranges accelerate the rate of fatigue life reduction, accentuating brittle failure. The relationship between fatigue life, corrosion degree, and survival probability under distinct stress ranges is shown in Fig. 20 [73]. Experimental data, in conjunction with measured data points, align around the median curve, predominantly falling within the 10% to 90% survival probability range. Nakamura and Suzumura [8] conducted fatigue tests on steel wires bearing artificial pits of various shapes, observing round, triangular, and triangular notched pit configurations. The pit shape emerged as a significant determinant, reducing fatigue strength notably due to higher SCFs. Triangular pits displayed lower fatigue strength compared to round counterparts. Furthermore, pit size significantly impacted the fatigue life of corroded steel wires, revealing a substantial

decrease when pit depths ranged from 0.2 to 0.6 mm, with a maximum reduction of 99.25% [74]. Interestingly, a marginal enhancement in fatigue life was noticed due to the superposition effect of pits. For instance, when the stress ratio transitioned from -1 to 0.44, steel wires with a 0.16 depth-width ratio of pits showcased a decline rate in its S-N curve more than double compared to steel wires featuring a 0.75 depth-width ratio of pits.

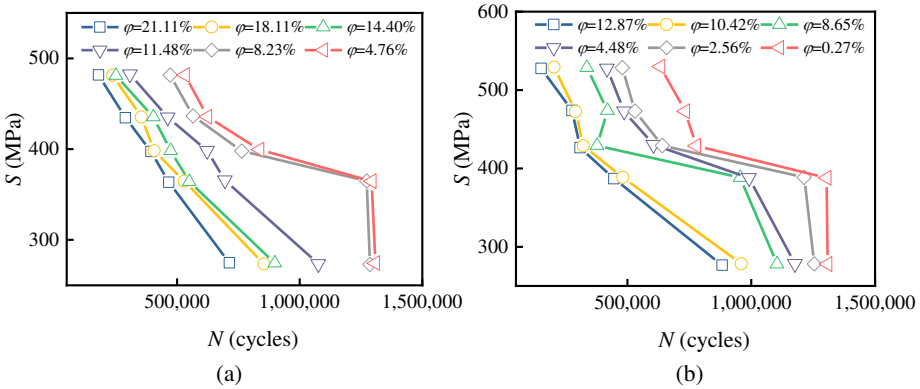

Fig. 19. S-N curves of Zn-coated steel wires (a) and Zn-Al alloy-coated steel wires (b) under different corrosion degrees [72].

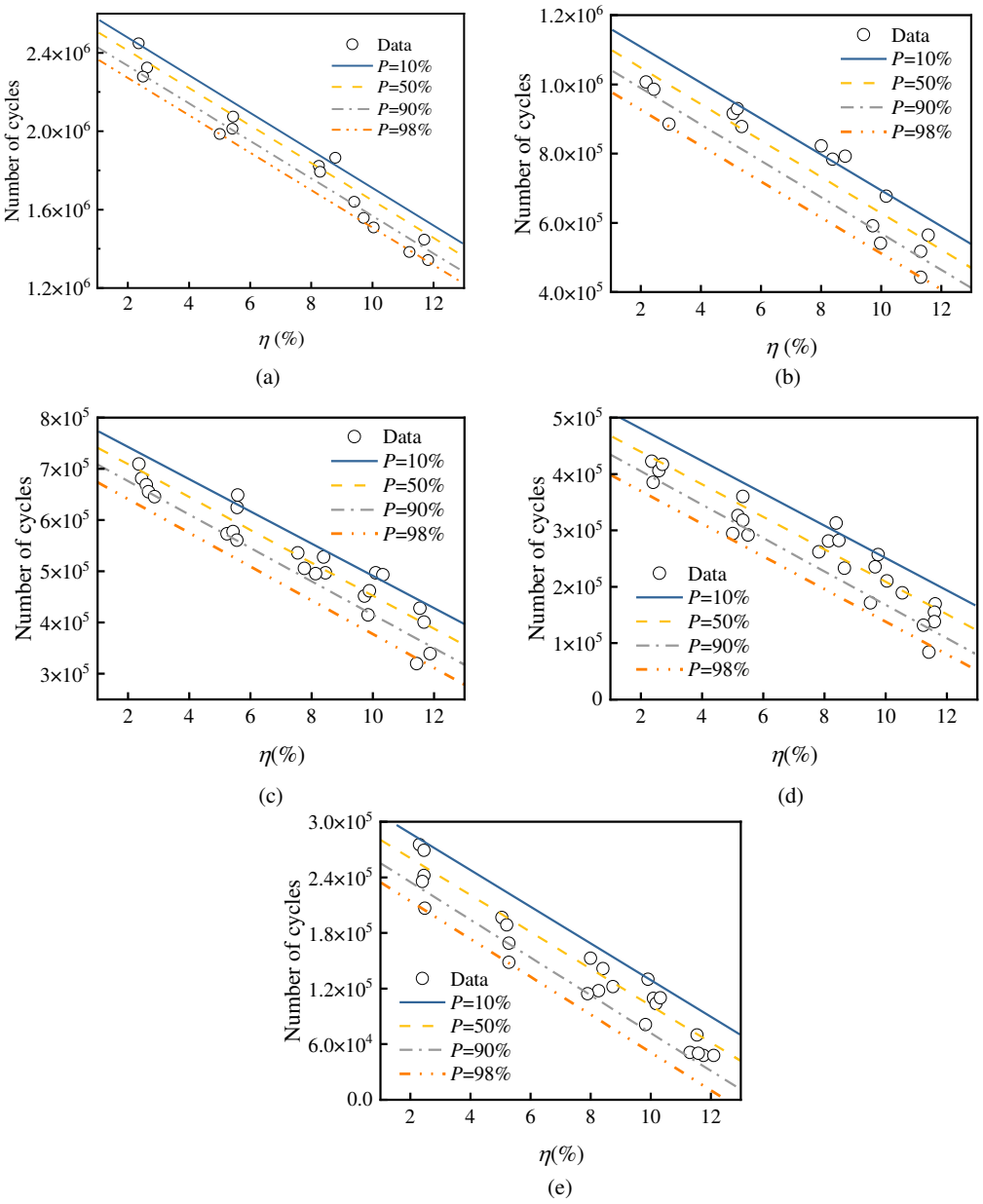

Fig. 20. Fatigue life vs. corrosion degree for steel wire. (a) $\Delta\sigma$=270MPa, (b) $\Delta\sigma$=360MPa, (c) $\Delta\sigma$=450MPa, (d) $\Delta\sigma$=540MPa, and (e) $\Delta\sigma$=630MPa [73].

The modified Manson-Coffin formula, considering both the average stress and the stress gradient, is introduced to predict the fatigue life of steel wire with pits [74]. The expressions are written as follows:

$$\begin{cases} \varepsilon_{\mathrm{a}} = \gamma \times \left[\dfrac{\sigma_{\mathrm{f}}' - \sigma_{\mathrm{m}}}{E} \left(2N\right)^{b^*} + \varepsilon_{\mathrm{f}}' \left(2N\right)^{c} \right] \\ \gamma = \dfrac{H^2}{W \times 2R \times \left(L+1\right)} \\ b^* = b + \dfrac{\lg\left(K_{\mathrm{t}}/K_{\mathrm{f}}\right)}{\lg 2 + 7} \approx b + 0.137 \lg\left(K_{\mathrm{t}}/K_{\mathrm{f}}\right) \end{cases} \tag{11}$$

where σ_{f}' is the fatigue strength coefficient, $\varepsilon_{\mathrm{f}}'$ is the fatigue continuity coefficient, b^* is the fatigue strength index considering the effect of stress gradient, γ is the correction factor, c is the fatigue ductility index, σ_{m} is the average stress, E is the elastic modulus, ε_{a} is the total strain, K_{t} is the SCF, and K_{f} is the fatigue notch factor. The fatigue notch coefficient K_{f} is calculated according to Peterson's formula, i.e.:

$$K_{\mathrm{f}} = 1 + \frac{K_{\mathrm{t}} - 1}{1 + a_{\mathrm{m}}/\rho} \tag{12}$$

where a_{m} is a constant related to the tensile strength of the material, and ρ is the radius of the notch root. The modified fatigue life for steel wires with corrosion pits more closely aligns with experimental results, achieving up to a 10% enhancement in accuracy over unmodified calculations. This modified formula notably improves the precision in predicting the fatigue life of steel wire affected by corrosion pits. The S-N curves of the mean line for uncorroded and corroded wires are fitted as the following [44]:

$$\Delta\sigma^{5.3} N = 10^{19.5} \quad \text{for un-corroded wires} \tag{13}$$

$$\Delta\sigma^{3.8} N = 10^{15.5} \quad \text{for corroded wires} \tag{14}$$

with the design line of S-N curves being as follows:

$$\Delta\sigma^{5.2} N = 10^{19.0} \quad \text{for un-corroded wires} \tag{15}$$

$$\Delta\sigma^{3.6} N = 10^{14.5} \quad \text{for corroded wires} \tag{16}$$

In a previous investigation, the authors employed the Theory of Critical Distances (TCD) to investigate notch fatigue in high-strength steel wires with corrosion pits [26, 27]. This method involved assessing fatigue by considering the maximum stress near the notch tip.

Schematically demonstrated in Fig. 21, the TCD offers various configurations applicable for analysis. Mathematically, the effective stress range $\Delta\sigma_{\text{eff}}$ is determined according to the following equations:

$$\Delta\sigma_{\text{eff}} = \Delta\sigma_y\left(\theta = 0, r = \frac{L}{2}\right) \ \left(\text{Point Method}\right) \tag{17}$$

$$\Delta\sigma_{\text{eff}} = \frac{1}{2L}\int_0^{2L} \Delta\sigma_y\left(\theta = 0, r\right) \ \left(\text{Line Method}\right) \tag{18}$$

$$\Delta\sigma_{\text{eff}} = \frac{4}{\pi L^2}\int_0^{\pi/2}\int_0^{L} \Delta\sigma_1\left(\theta, r\right)\cdot r \cdot \mathrm{d}r \cdot \mathrm{d}\theta \ \left(\text{Area Method}\right) \tag{19}$$

In Eqs (17)-(19), critical distance L_{T}, a function of materials and load ratios, is determined via the SIF threshold, ΔK_{th}, and the plain fatigue limit range, $\Delta\sigma_0$, as follows:

$$L_{\text{T}} = \frac{1}{\pi}\left(\frac{\Delta K_{\text{th}}}{\Delta\sigma_0}\right)^2 \tag{20}$$

The theory assumes that critical distance L increases with the increase of the number of cycles to failure N, defined through the following simple power law [75]:

$$L\left(N\right) = A\cdot N^B \tag{21}$$

where A and B are material constants determined via specific calibration fatigue tests. These constants vary with different materials and load ratios. A and B are determined using the critical distance value under static loading L_{S} as well as the high-cycle critical distance value L_{T}. L_{S} is defined as:

$$L_{\text{S}} = \frac{1}{\pi}\left(\frac{K_{\text{Ic}}}{\sigma_{\text{b}}}\right)^2 \tag{22}$$

where K_{Ic} is the plane strain fracture roughness and σ_{b} is the tensile strength. Given an initial value of the number of cycles to failure N_i, Eq. (21) yields the corresponding critical distance:

$$L\left(N_i\right) = A\cdot N_i^B \tag{23}$$

The stress range $\Delta\sigma_{1i}$ at a distance from the notch tip equal to $L(N_i)/2$ is determined by the linear-elastic stress field. From the S-N curve of the plain material, the stress range is subsequently used to recalculate the number of cycles to failure as follows:

$$N_j = N_A \left(\frac{\Delta\sigma_A}{\Delta\sigma_{1i}} \right)^n \tag{24}$$

where n and $\Delta\sigma_A$ are the negative inverse slope and the reference stress range at N_A cycles to failure of the plain fatigue curve, respectively (Fig. 22). If N_j is not equal to the assumed initial value N_i, then the above procedure has to be reapplied by imposing $N_i = N_j$, reiterating it until convergence occurs.

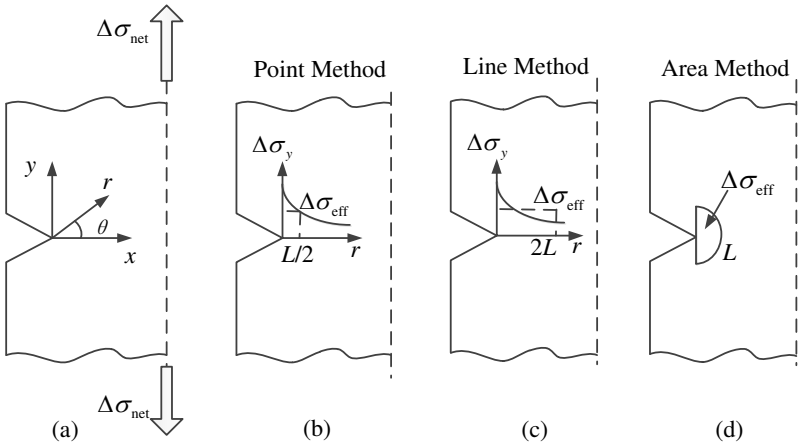

Fig. 21. (a) Local system of coordinate; (b) The Theory of Critical Distances according to the Point Method; (c) the Line Method; (d) the Area Method [28].

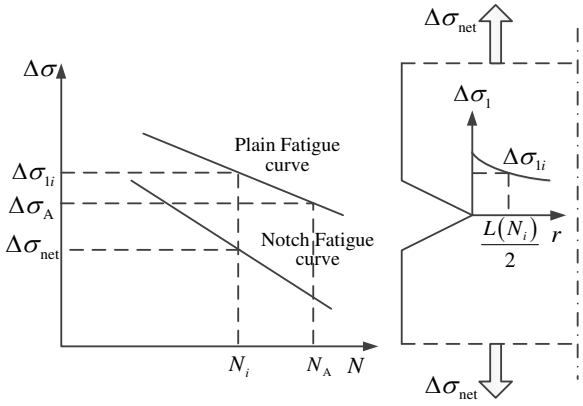

Fig. 22. Determination of the critical distance value using two calibration fatigue curves [29].

In short, the fatigue behavior of corroded steel wires undergoes significant shifts

influenced by various factors like corrosion degree, pit shape and size, stress range, stress ratio, and wire types, as seen through S-N curves and fatigue tests. Advanced approaches like the modified Manson-Coffin formula and the TCD have notably improved the accuracy in predicting the fatigue life in these wires, enhancing our understanding of how these wires behave under different stress conditions and corrosion scenarios. Overall, these studies emphasize the complex interplay of factors impacting fatigue in corroded steel wires and the efficacy of refined models in better predicting their fatigue behavior. However, the stress-based approach inadequately elucidates the mechanisms underlying corrosion fatigue crack initiation and propagation. Incorporating environmental parameters, such as temperature, humidity, and corrosive media, into stress-based models is essential as these factors significantly influence corrosion fatigue processes.

4.2. Energy method

The energy-based method for fatigue assessment in notched components has gained increasing attention, particularly the Strain Energy Density (SED) method proposed by Lazzarin et al. [76] for sharp and blunt notches. This approach assumes that failure occurs when the averaged SED within a defined volume reaches a critical value as a material property. Employing stress components, it computes the Mode I and Mode II notch stress intensity factors (NSIF) according to the following standard definitions (Fig. 23):

$$K_1 = \sqrt{2\pi}\lim_{r\to 0^+} r^{1-\lambda_1}\sigma_{\theta\theta}\left(r,\theta=0\right) \tag{25}$$

$$K_2 = \sqrt{2\pi}\lim_{r\to 0^+} r^{1-\lambda_2}\tau_{r\theta}\left(r,\theta=0\right) \tag{26}$$

where r and θ represent the local polar coordinate, $\sigma_{\theta\theta}$ and $\tau_{r\theta}$ denote the stress components, λ_1 and λ_2 are Williams' eigenvalues depending on the notch opening angle 2α, and K_1 and K_2 are Mode I and Mode II NSIFs, respectively. The total elastic strain energy density for an isotropic material is expressed as:

$$W = \frac{1}{2E}\left[\sigma_{11}^2+\sigma_{22}^2+\sigma_{33}^2-2\nu\left(\sigma_{11}\sigma_{22}+\sigma_{11}\sigma_{33}+\sigma_{22}\sigma_{33}\right)+2\left(1+\nu\right)\sigma_{12}^2\right] \tag{27}$$

where σ_{11}, σ_{22}, σ_{33} and σ_{12} denote stress components. This leads to the evaluation of the

averaged SED within a control volume surrounding the notch tip (Fig. 24):

$$\bar{W} = \frac{1}{E}\left[e_1 \cdot \frac{K_1^2}{R_0^{2(1-\lambda_1)}} + e_2 \cdot \frac{K_2^2}{R_0^{2(1-\lambda_2)}} \right] \tag{28}$$

where R_0 represents the radius of the control volume, and e_1 and e_2 are shape functions related to the notch opening angle, 2α, and Poisson's ratio, ν. The control radius R_0 is estimated through the following expression [77]:

$$R_0 = \left(\frac{\sqrt{2e_1}\Delta K_{1A}}{\Delta \sigma_A} \right)^{\frac{1}{1-\lambda_1}} \tag{29}$$

where ΔK_{1A} and $\Delta \sigma_A$ are the reference values of the NSIF and the nominal stress range of plain components, respectively. In the case of a blunt notch (circular or elliptical holes, etc.), the maximum principal stress at the notch tip characterizes the averaged SED. This is expressed as:

$$\bar{W} = \left(\frac{I_1}{2\Omega} \right) r_0^{2(1-\lambda_1)} \left[\frac{\sqrt{2\pi}}{1+\tilde{\omega}_1} \right]^2 \frac{\sigma_{mps}^2}{E} = F(2\alpha) H\left(2\alpha, \frac{R_0}{\rho} \right) \frac{\sigma_{mps}^2}{E} \tag{30}$$

where

$$F(2\alpha) = \left(\frac{q-1}{q} \right)^{2(1-\lambda_1)} \left[\frac{\sqrt{2\pi}}{1+\tilde{\omega}_1} \right]^2 \tag{31}$$

$F(2\alpha)$ depends on the notch opening angle, H is a function of the notch opening angle and Poisson's ratio, ρ is the notch radius, and σ_{mps} is the maximum principal stress.

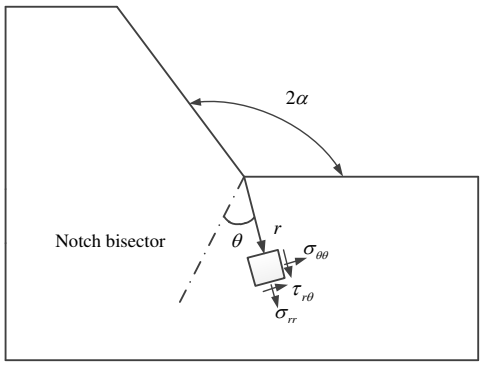

Fig. 23. Local coordinate system and stress components for a sharp notch [29].

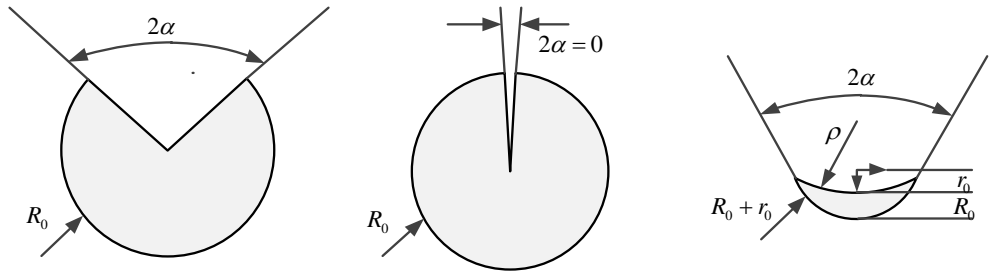

Fig. 24. Control volume for sharp V-notch, crack, and blunt V-notch [29].

Li et al. [28] use the dual scale SED factor range to describe the FCG rate as follows:

$$\frac{\mathrm{d}a}{\mathrm{d}N} = C_0 \left(\Delta S_{\text{micro}}^{\text{macro}} \right)^m \tag{32}$$

$$\Delta S_{\text{micro}}^{\text{macro}} = \frac{2\left(1-2\nu_{\text{micro}}\right)\left(1-\nu_{\text{macro}}\right) a \sigma_{\text{a}} \sigma_{\text{m}}}{\mu_{\text{macro}}} \mu^* \left(1-\sigma^*\right)^2 \sqrt{d^*} \sqrt{\frac{d_0}{r}} \tag{33}$$

where

$$\mu^* = \frac{\mu_{\text{micro}}}{\mu_{\text{macro}}},\ \sigma^* = \frac{\sigma_0}{\sigma_\infty},\ d^* = \frac{d}{d_0} \tag{34}$$

$$\sigma_{\text{a}} = \frac{\sigma_{\max} - \sigma_{\min}}{2},\ \sigma_{\text{m}} = \frac{\sigma_{\max} + \sigma_{\min}}{2} \tag{35}$$

Here, ν_{micro} and ν_{macro} are the microscopic and macroscopic Poisson's ratios respectively, μ_{micro} and μ_{macro} are the microscopic and macroscopic shear moduli, a is the crack depth, r is a distance measured from the crack tip, σ_{a} is the stress amplitude, $\sigma_{\max}$ and $\sigma_{\min}$ are the maximum and minimum stresses, respectively, d^*, μ^* and σ^* are defined by Eq. (34) which reflects the influences of both macroscopic and microscopic effects.

Furthermore, the concept of an energy release rate is applied to depict the FCG, as described by the authors in Fig. 25 [25]. G_{th}, G_{pl}, and G_{c} represent the energy release rate threshold, the upper limit of the energy release rate, and the critical value of the energy release rate, respectively. The equation suitable for estimating fatigue crack initiation is given by：

$$\frac{N}{c_1 (\Delta G)^{c_2}} \geq 1.0 \tag{36}$$

where c_1 and c_2 are material parameters for fatigue crack initiation. The FCG rate, a

function of the energy release rate range, is expressed as follows:

$$\frac{\mathrm{d}a}{\mathrm{d}N} = c_3 \left(\Delta G\right)^{c_4} \tag{37}$$

where c_3 and c_4 are FCG parameters. Based on the relationship between ΔG and ΔK, the expressions of c_3 and c_4 can be presented as follows:

$$c_3 = C\left(E'\right)^{c_4} \tag{38}$$

$$c_4 = m/2 \tag{39}$$

where

$$E' = \begin{cases} E & \text{Plane stress} \\ \dfrac{E}{1-\nu^2} & \text{Plane strain} \end{cases} \tag{40}$$

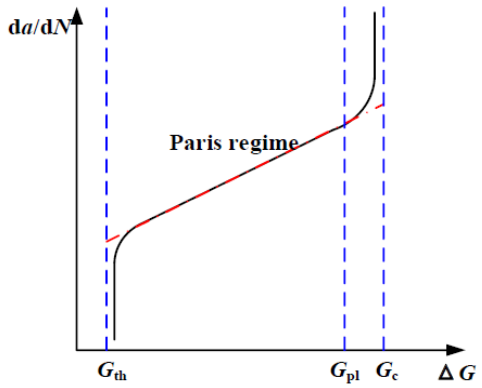

Fig. 25. Relationship between FCG rate and energy release rate [25].

The SED method emerges as a promising tool for evaluating fatigue strength in notched components, especially in corroded metallic steel wires, leveraging stress components and NSIFs. The accuracy of this method hinges on factors like the NSIF and the control radius, pivotal in assessing fatigue in both sharp and blunt notches. Dual-scale strain energy density factors employed to describe the FCG rate offer a nuanced understanding, considering both microscopic and macroscopic influences. Additionally, the FCG rate as a function of the energy release rate provides valuable insights into material behavior under cyclic loading. However, the energy method involves a complex calculation process with numerous parameters to be determined, leading to a relatively cumbersome procedure. To streamline

the calculation process without compromising accuracy, it is advisable to devise empirical models or simplified approaches grounded in either experimental data or theoretical insights.

4.3. Fracture mechanics method

According to section 2.1, a three-stage multiscale corrosion fatigue evolution process involves pitting formation and growth, short crack propagation, and long crack propagation. The electrochemical process induced irreversible damage to the crystal plane and resulted in the initiation of pitting. If pitting develops at a constant volume growth rate after initiation, according to Faraday's law, the expression of pitting growth rate can be written as [78]:

$$\frac{\mathrm{d}V}{\mathrm{d}t} = \frac{MI_{\mathrm{P0}}}{nF\rho}\exp\left(-\frac{\Delta H}{R_{\mathrm{g}}T}\right) \tag{41}$$

where V is the pit volume, M is the molar mass, I_{P0} is the pitting current coefficient, n is the number of released electrons, F is the Faraday constant, ρ is the material density, ΔH is the activation energy variable per unit volume, and R_{g} is the gas constant, and T is the absolute temperature. The corrosion pit typically has a semi-ellipsoid shape, with the pit volume being expressed as:

$$V = \frac{2}{3}\pi\varphi^2 a_{\mathrm{p}}^3 = \frac{MI_{\mathrm{P0}}}{nF\rho}\exp\left(-\frac{\Delta H}{R_{\mathrm{g}}T}\right)t_{\mathrm{pit}} \tag{42}$$

where $\varphi=b_{\mathrm{p}}/a_{\mathrm{p}}$ is the morphology characteristics of the corrosion pit (ratio of width to depth). Considering the acceleration effect of the cyclic traffic load on the corrosion process, and combining Eqs. (41) and (42), the duration of the pit initiation stage can be represented as:

$$t_{\mathrm{pt}} = \frac{2\pi\varphi^2 a_{\mathrm{p}}^3 nF\rho}{3MI_{\mathrm{P0}}\exp\left(-\dfrac{\Delta H}{R_{\mathrm{g}}T}\right)C_{\mathrm{P}}^{3\Delta\sigma}} \tag{43}$$

where C_{p} is a constant. The transformation from pits to cracks satisfied the SIF criterion:

$$\Delta K_{\mathrm{pit}} \geq \Delta K_{\mathrm{th}} \tag{44}$$

where ΔK_{pit} is the SIF range, and ΔK_{th} is the SIF threshold of the short crack. The critical

size for the conversion of pits to cracks can be determined using Eq. (44).

Paris' law is a widely used empirical equation for modeling FCG during the stable growth stage. Sih et al. [79] established the FCG sigmoidal curves for high-strength steel:

$$\text{Region I}:\left(\frac{\mathrm{d}a}{\mathrm{d}N}\right)_{\mathrm{I}}=C_{\mathrm{I}}\left(\Delta K\right)^{m_{\mathrm{I}}},\ \log\left(\mathrm{d}a/\mathrm{d}N\right)_{\mathrm{I}}<-4.09\ \text{mm/cycle} \tag{45}$$

$$\text{Region II}:\left(\frac{\mathrm{d}a}{\mathrm{d}N}\right)_{\mathrm{II}}=C_{\mathrm{II}}\left(\Delta K\right)^{m_{\mathrm{II}}},\ -4.09\le\log\left(\mathrm{d}a/\mathrm{d}N\right)_{\mathrm{II}}\le-3.30\ \text{mm/cycle} \tag{46}$$

$$\text{Region III}:\left(\frac{\mathrm{d}a}{\mathrm{d}N}\right)_{\mathrm{III}}=C_{\mathrm{III}}\left(\Delta K\right)^{m_{\mathrm{III}}},\ \log\left(\mathrm{d}a/\mathrm{d}N\right)_{\mathrm{III}}>-3.30\ \text{mm/cycle} \tag{47}$$

where C_{I}, m_{I}, C_{II}, m_{II}, C_{III}, and m_{III} are FCG parameters for region I, region II, and region III, respectively (Fig. 26). Jiang et al. [80] identified a two-stage FCG rate for high-strength cold-drawn eutectoid steel wires, revealing changes based on stress ratios (Fig. 27). Additionally, the FCG equation is expressed as follows:

$$\frac{\mathrm{d}a}{\mathrm{d}N}=C\cdot\left(\Delta K_{\mathrm{eff}}\right)^{m} \tag{48}$$

where ΔK_{eff} is the effective SIF range defined as:

$$\Delta K_{\mathrm{eff}}=\begin{cases}K_{\max}-K_{\mathrm{open}} & \text{if } K_{\mathrm{open}}\ge K_{\min}\\ K_{\max}-K_{\min} & \text{if } K_{\mathrm{open}}<K_{\min}\end{cases} \tag{49}$$

where $K_{\max}$, $K_{\min}$, and K_{open} are the maximum, minimum, and crack opening SIF, respectively. K_{open} is a function of stress ratio R and is given by:

$$\frac{K_{\mathrm{open}}}{K_{\max}}=\begin{cases}\max\left(R,A_0+A_1R+A_2R^2+A_3R^3\right) & \text{if } R\ge0\\ A_0+A_1R & \text{if } R<0\end{cases} \tag{50}$$

where A_0, A_1, A_2, and A_3 are constants that can be expressed as follows [81]:

$$\begin{cases}A_0=\left(0.825-0.34\alpha+0.05\alpha^2\right)\left(\cos\dfrac{\pi\sigma_{\max}}{2\sigma_0}\right)^{1/\alpha}\\ A_1=\left(0.415-0.071\alpha\right)\cdot\left(\dfrac{\sigma_{\max}}{\sigma_0}\right)\\ A_2=1-A_0-A_1-A_3\\ A_3=2A_0+A_1-1\end{cases} \tag{51}$$

Here, σ_0 is the flow stress and α is the constraint stressor.

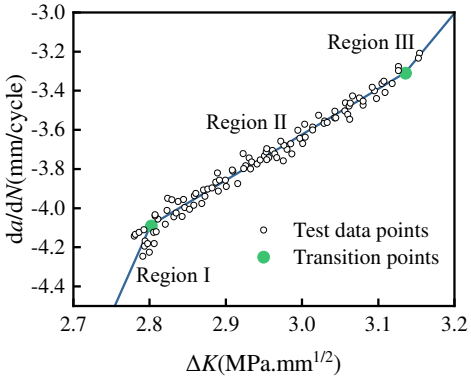

Fig. 26. Three-stage FCG rate [79].

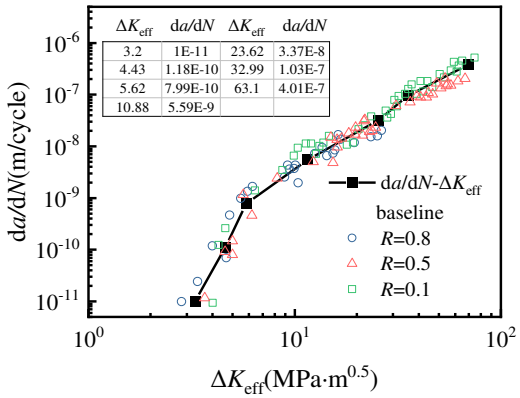

Fig. 27. Two-stage FCG rate [80].

Acknowledging the acceleration effect of the corrosion environment on crack growth, the introduction of the crack growth corrosion acceleration factor, C_{corr}, aligned with Paris' law, defines the short crack growth stage as:

$$\frac{\mathrm{d}a}{\mathrm{d}N} = C_{\text{corr}} C_{\text{sc}} \left(\Delta K\right)^{m_{\text{sc}}} \tag{52}$$

where C_{sc} and m_{sc} are short fatigue crack propagation parameters. The duration of the short crack growth stage is expressed as:

$$t_{\text{sc}} = \frac{1}{f} \int_{a_{\text{sc}}}^{a_{\text{tr}}} \frac{1}{C_{\text{corr}} C_{\text{sc}} \left(\Delta K\right)^{m_{\text{sc}}}} \mathrm{d}a \tag{53}$$

where a_{tr} is the critical size of transition from short crack to long crack. It is assumed that C_{corr} is consistent between the short and long crack growth stages. The long crack growth stage is then described as:

$$\frac{\mathrm{d}a}{\mathrm{d}N_{\mathrm{lc}}} = C_{\mathrm{corr}} C_{\mathrm{lc}} \left(\Delta K\right)^{m_{\mathrm{lc}}} \tag{54}$$

where C_{lc} and m_{lc} are long fatigue crack propagation parameters. The expression of the duration of the long crack growth stage is written as:

$$t_{\mathrm{lc}} = \frac{1}{f} \int_{a_{\mathrm{tr}}}^{a_{\mathrm{f}}} \frac{1}{C_{\mathrm{corr}} C_{\mathrm{lc}} \left(\Delta K\right)^{m_{\mathrm{lc}}}} \mathrm{d}a \tag{55}$$

where a_{f} is the critical size for the long crack to grow to failure. The corrosion factor as a function of corrosion depth is fitted by test data [82]:

$$C_{\mathrm{corr}} = 0.5356 \cdot d + 1 \tag{56}$$

where d is the corrosion depth (mm). Martín and Sánchez-Gálvez [83] proposed a parametric model accounting for the impact of waveforms, frequencies, and stress ratios on the corrosion fatigue behavior of prestressing steels in seawater.

Summarily, pitting evolves at a rate governed by Faraday's law, with its growth rate and volume determined by various factors including the pitting current coefficient and material properties. Transitioning from pits to cracks adheres to the SIF criterion. The evolution of FCG has been elucidated by empirical models like Paris' law, while diverse studies have shed light on the intricate variations in fatigue behavior under different stress conditions. An improved and unified three-staged FCG model has been proposed, enhancing accuracy in assessment. Researchers have expanded models to encompass factors like crack closure, corrosion, and stress ratio, showcasing the depth of considerations essential for a holistic fatigue assessment. It introduces a corrosion acceleration factor to quantify the influence of the corrosive environment on both short and long crack growth stages, using parameters fitted from experimental data. These varied approaches collectively contribute to a comprehensive understanding of material degradation, providing insights crucial for ensuring structural integrity in diverse operating conditions and environments. However, determining the initial crack size presents a challenge, significantly impacting the precision of fatigue life prediction. Calibrating fatigue life prediction models using experimental data

or field measurements helps to account for variations in initial crack size and enhances prediction accuracy.

4.4. Damage mechanics method

Damage mechanics provides a valuable framework for modeling the progression and evolution of corrosion fatigue in high-strength steel wires. A damage variable, denoted as D, delineates the gradual reduction in effective cross-sectional area A_e due to material degradation [32]:

$$D = 1 - A_e / A_0 \tag{57}$$

where A_0 represents the original cross-sectional area. Subsequently, the effective stress σ_e is defined as a function of the nominal stress σ:

$$\sigma_e = \sigma / (1 - D) \tag{58}$$

A simplified elastic damage evolution model and a plastic damage evolution model have been proposed for steel wires as follows [2]:

$$\frac{\mathrm{d}D_e}{\mathrm{d}N} = D_e^{\alpha} \left(\frac{\sigma_a}{2M_0} \right)^{\beta} \tag{59}$$

$$\frac{\mathrm{d}D_p}{\mathrm{d}N} = \left(\frac{\Delta\varepsilon}{\varepsilon_0} + 1 \right) \cdot D_p^{\alpha} \left(\frac{\sigma_a}{2M_0} \right)^{\beta} \tag{60}$$

where α, β, and M_0 are material constants, ε_0 is the maximum elastic strain, and $\Delta\varepsilon$ is the accumulated plastic strain. Xue and Shen [84] propose another evolution equation of corrosion fatigue damage:

$$\frac{\mathrm{d}D}{\mathrm{d}t} = \frac{\mathrm{d}D_c}{\mathrm{d}t} + \frac{\mathrm{d}D_{scc}}{\mathrm{d}t} + \frac{\mathrm{d}D_s}{\mathrm{d}t} \tag{61}$$

$$\frac{\mathrm{d}D_c}{\mathrm{d}t} = \frac{c_0 + c_1 (\sigma_m + \sigma_a)^{\alpha}}{(1 - D)^m} \tag{62}$$

$$\frac{\mathrm{d}D_{scc}}{\mathrm{d}t} = c_{scc} \left(\frac{\sigma_m}{1 - D} \right)^{\beta} K \tag{63}$$

$$\frac{\mathrm{d}D_{\mathrm{s}}}{\mathrm{d}N}=\left(1-D\right)^{-u}\left[\frac{\sigma_{\mathrm{a}}}{M\left(\sigma_{\mathrm{m}}\right)}\right]^{\omega} \tag{64}$$

$$K=\begin{cases}1-\left[\dfrac{\left(1-D\right)\sigma_{\mathrm{scc}}}{\sigma_{\mathrm{m}}}\right]^{\gamma}, & \dfrac{\sigma_{\mathrm{m}}}{1-D}>\sigma_{\mathrm{scc}}\\ 0 \quad , & \text{others}\end{cases} \tag{65}$$

where D_{c} is the structural damage caused by corrosion, D_{scc} is the stress corrosion damage caused by average stress, D_{s} is the fatigue damage caused by the stress range, t is time, T_0 is the period of fatigue load, c_0 is the damage accumulation factor under no stress condition, m is the damage coefficient caused by the corrosion, $c_1\left(\sigma_{\mathrm{m}}+\sigma_{\mathrm{a}}\right)^{\alpha}$ is the accelerated effect of stress on corrosion damage, α is a constant related to materials, c_{scc} is the cumulative coefficient of stress corrosion damage, σ_{scc} is the threshold value of stress corrosion, γ is a constant related to the material, u and ω are experimental constants, and $M\left(\sigma_{\mathrm{m}}\right)$ is the material parameter related to the average stress.

A numerical method is applied to simulate the corrosion fatigue process, as plotted in Fig. 28 [32]. Initially, a finite element model with corrosion pits is established under dynamic fatigue loading blocks. This method computes stress time histories for all elements, enabling the determination of damage increment $\Delta D_{\mathrm{CF}}^{e}\left(t\right)$ according to the following equations:

$$D_{\mathrm{CF}}^{e}\left(t\right)=D_{\mathrm{CF}}^{e}\left(t\right)-D_{\mathrm{CF}}^{e}\left(t-\Delta t\cdot\Delta T\right)=\frac{\partial D_{\mathrm{CF}}\left(t-\Delta t\cdot\Delta T\right)}{\partial t}\Delta t\cdot\Delta T \tag{66}$$

where

$$D_{\mathrm{CF}}\left(t\right)=\begin{cases}\sqrt{D_{\mathrm{F}}\left(t\right)}+\alpha_{\mathrm{c}}t^{\beta_{\mathrm{c}}}/R, & t\le t_{\mathrm{p}}\\ \sqrt{D_{\mathrm{F}}\left(t\right)}+\left\{\left[\dfrac{x_{\mathrm{c}}^{(1-q)}}{1-q}+C\sigma^{p}\left(t-t_{\mathrm{p}}\right)\right]\left(1-q\right)\right\}^{1/(1-q)}\Big/R, & t>t_{\mathrm{p}}\end{cases} \tag{67}$$

$$D_{\mathrm{F}}\left(t\right)=\left\{\left(1-\alpha_{\mathrm{f}}\right)\left[\frac{\Delta\sigma}{2M_{0}}\right]^{\beta_{\mathrm{f}}}tf\right\}^{\frac{1}{1-\alpha_{\mathrm{f}}}} \tag{68}$$

here, α_{c}, β_{c}, α_{f}, β_{f}, C, p, q, and M_0 are the model parameters, x_{c} is the critical pit-to-

crack transition size, and $D_{\mathrm{F}}(t)$ is damage accumulation. Subsequently, it determines whether the element failed, and then updates the stiffness matrix.

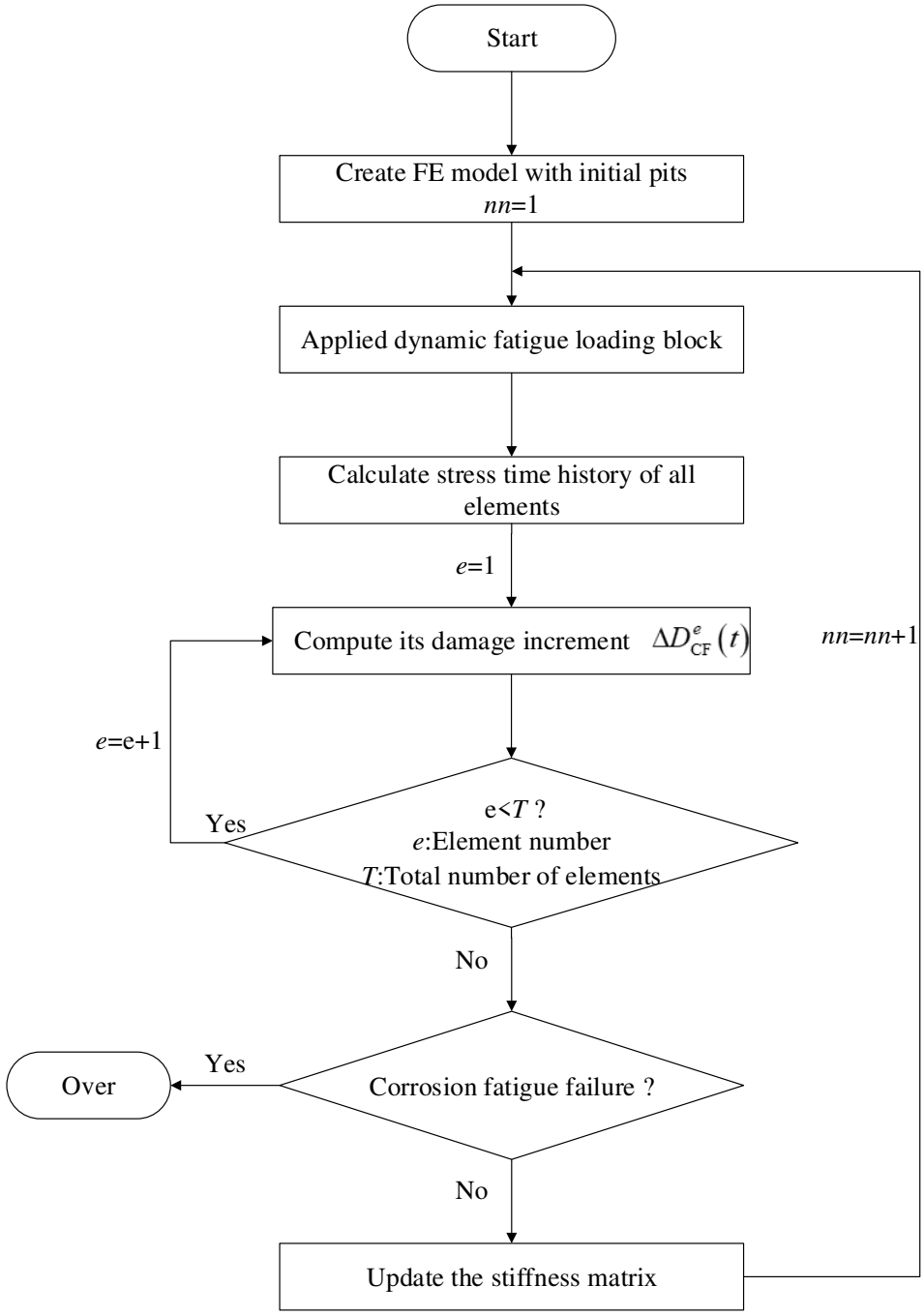

Fig. 28. Flow chart of the corrosion fatigue damage simulation algorithm [32].

Wang et al. [85, 86] delved into the corrosion fatigue performance of corroded steel wires, examining single and multiple pits. Their investigation revealed a progression in damage evolution and stress distribution within notched wires under fatigue loading, depicted in

Figs. 29-31. Initially, stress concentration starts at the notch center, leading to damage accumulation, which extends beyond the notch as the load increases. Despite reduced material stiffness around the notch, damaged areas retain stress transfer capability, transmitting higher stress to neighboring elements. In later stages, varying damage levels near and away from the notch cause stress redistribution. The corrosion pits initiate stress concentration and, under cyclic loading and corrosive environments, damage accumulates and spreads throughout the wire, altering stress distribution. The declining elastic modulus near the pit, causing local stiffness reduction, contributes to stress variations within and around the corrosion pit area.

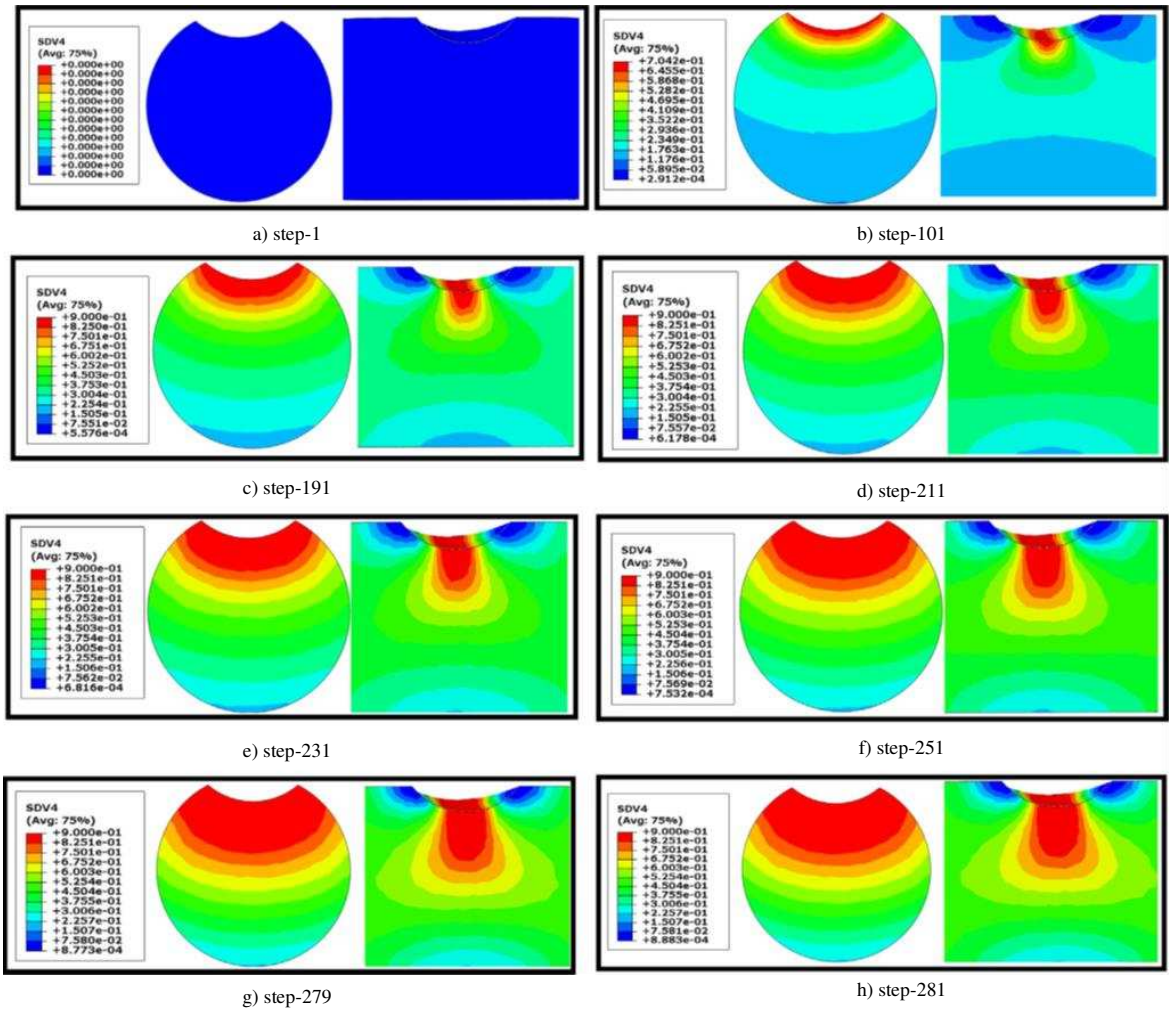

Fig. 29. The damage evolution of notched wires with a single pit under a fatigue load of 360MPa [85].

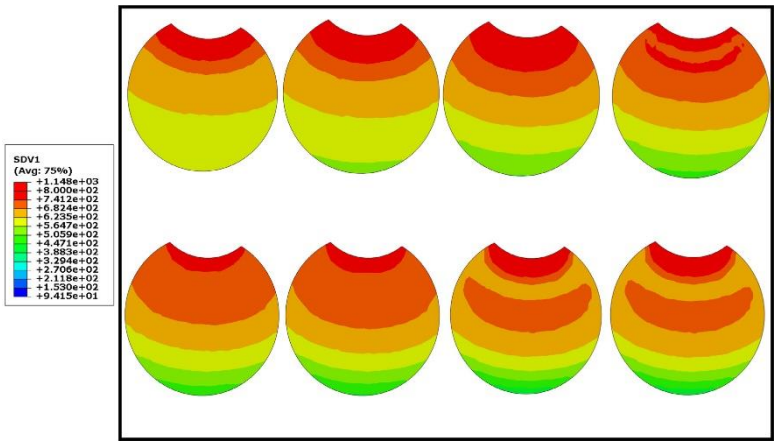

Fig. 30. The stress distribution of notched wires with a single pit under a fatigue load of 360MPa [85].

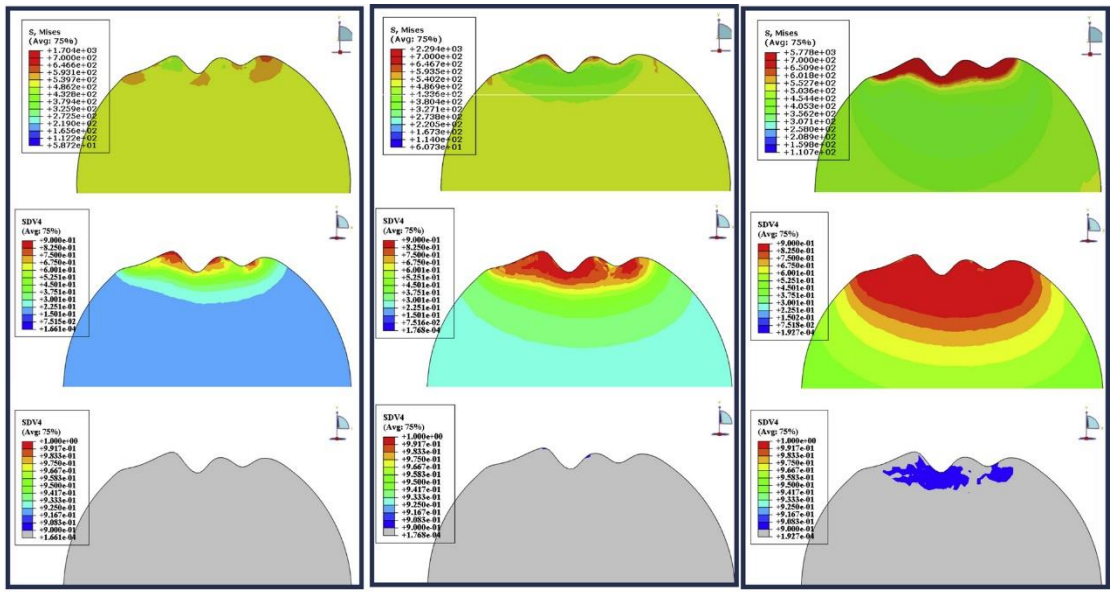

a) step=61 b) step=121 c) step=181

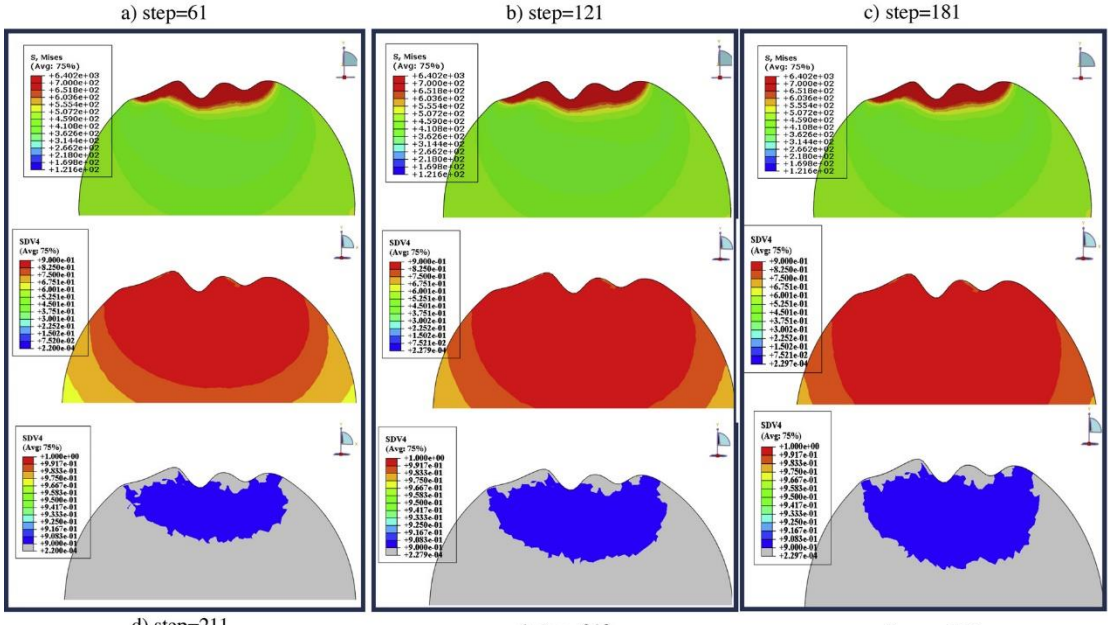

d) step=211 e) step=219 f) step=221

Fig. 31. The stress and damage distribution of notched wires with multiple pits under corrosion fatigue loading [86].

In short, the use of damage mechanics offers a framework to model the corrosion fatigue progression in high-strength steel wires, employing a variable to represent the reduction in the effective cross-sectional area due to material degradation. Various models like elastic, plastic, and corrosion-fatigue damage models capture the complex mechanisms involved in cyclic loading and corrosive environments. These models aim to simulate the intricate process of corrosion fatigue, including stress redistribution and damage evolution. However, it is difficult to obtain damage variables, and quantifying the damage process requires determining a large number of parameters through experiments. It develops simplified models that capture essential aspects of the damage process while minimizing the number of parameters required for calibration.

4.5. Data-driven method

There are many factors influencing corrosion fatigue, including material type, stress range, stress concentration, loading frequency, stress ratio, geometric size, corrosive medium, metallurgical composition, and so on [87]. Traditional methodologies face challenges in adequately addressing the multifaceted impact of all pertinent factors. Recently, many researchers have consistently demonstrated that the machine learning method represents a highly efficient approach for predicting fatigue life [88, 89].

However, limited research has addressed the corrosion fatigue behavior of components through data-driven methodologies. Dourado and Viana [90] devised a physics-informed neural network model to fill in missing physics within cumulative damage models. They demonstrated its efficacy in predicting corrosion fatigue of aircraft wing panels made of Al 2024-T3 alloy subjected to cyclic loading and saline corrosion. Feng et al. [91] proposed Borderline-SMOTE and XGBoost algorithms for predicting corrosion fatigue life. It enhanced prediction accuracy and generalization ability compared to existing models. Yu et al. [92] investigated the SCF in aluminum alloy 7075-T651 affected by pit sizes using data-driven models, analyzing fatigue performance through fracture mechanics theory. Their

results highlight the minor error and enhanced robustness, enabling accurate SCF predictions for the neural network. The SCF increases with pit length and width but decreases with pit depth, emphasizing the pivotal role of pit depth in influencing fatigue life. Ma et al. [68] introduce a data-driven Gaussian process regression method to predict the SCF induced by corrosion pits, employing a finite element model to generate suitable samples for Gaussian process regression (GPR) machine learning, as described in Fig. 32. This method enables probabilistic estimation of the SCF. Feng et al. [93] propose an enhanced approach for predicting corrosion fatigue life using Borderline-SMOTE and XGBoost algorithms, demonstrating excellent prediction accuracy and generalization under various factors. It reveals that the corrosive environment has the most significant impact, substantially larger than stress ratio, frequency, material strength, load type, joint type, surface state, and temperature.

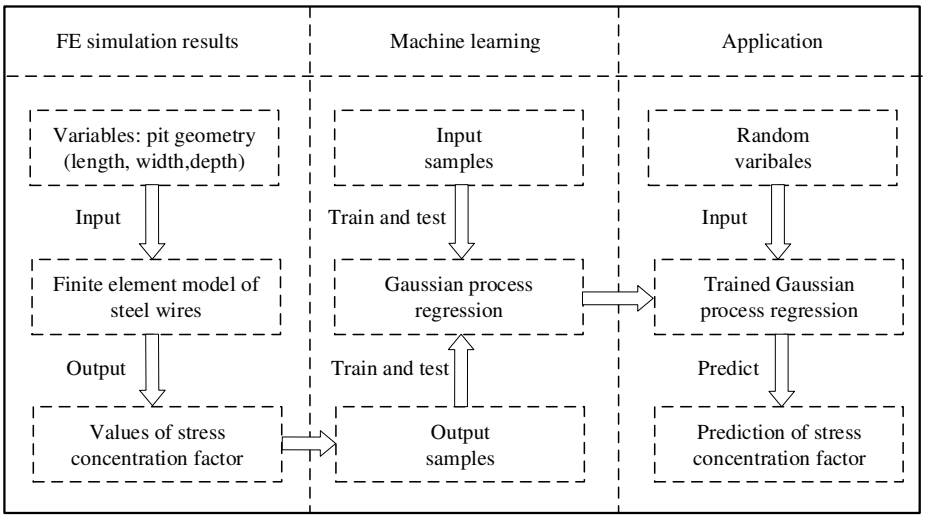

Fig. 32. The calculation process of the SCF of steel wires via machine learning [68].

Additionally, Guo et al. [94] propose a predictive machine learning-based model to assess the effect of corrosion degree, stress range, loading ratio, loading frequency, and other factors on the fatigue life for corroded high-strength steel wires. The corrosion degree significantly influences the relationship between fatigue life and stress range. To evaluate the performance of the model, three indexes were utilized: root-mean-squared error (*RMSE*), mean absolute error (*MAE*), and coefficient of determination (R^2), described as follows:

$$RMSE = \sqrt{\frac{\sum_{i=1}^{n}\left(P_i^{pred} - P_i^{true}\right)^2}{n}} \tag{69}$$

$$MAE = \frac{\sum_{i=1}^{n}\left|P_i^{pred} - P_i^{true}\right|}{n} \tag{70}$$

$$R^2 = 1 - \frac{\sum_{i=1}^{n}\left(P_i^{pred} - P_i^{true}\right)^2}{\sum_{i=1}^{n}\left(P_i^{pred} - \bar{P}_i^{true}\right)^2} \tag{71}$$

where the superscript 'pred' and 'true' on the ith fatigue life sample P_i denote the predicted and actual value, respectively, $\bar{P}_i^{true}$ is the average value of all samples, and n is the total number of the database samples. The study highlights an overfitting issue with SVR and ANN models. The improvements of the AdaBoost model over other models are calculated and given in Fig. 33. Comparatively, AdaBoost demonstrated marked improvements over other models, displaying significant enhancements in MAE and RMSE by approximately 50% when contrasted with SVR and ANN. These findings underscore the superior predictive capability of the AdaBoost method in determining the fatigue performance of corroded wires.

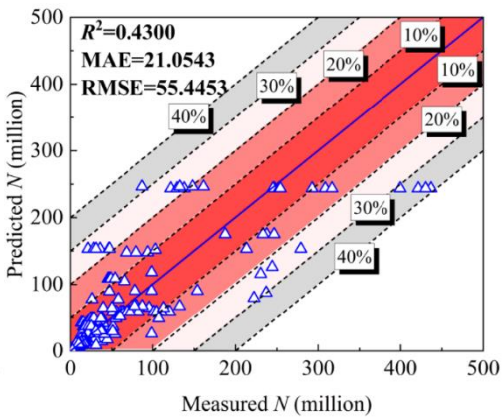

(a)

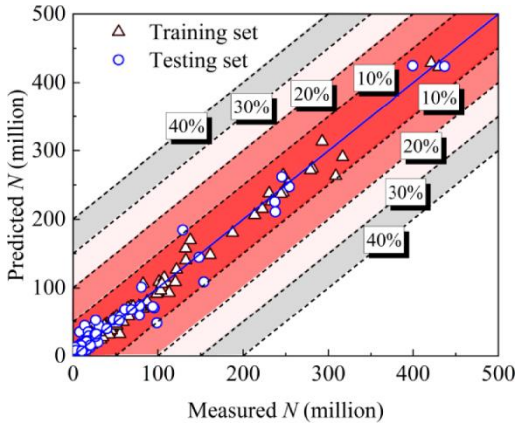

(b)

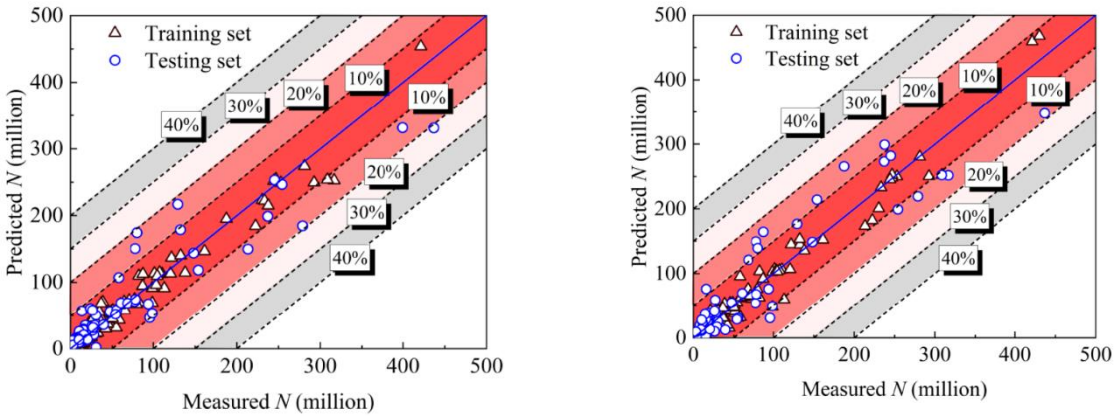

(c) (d)

Fig. 33. Predicted life versus measured life: (a) empirical formulas, (b) AdaBoost, (c)SVR, and (d)ANN [94].

In conclusion, this study underscores machine learning's pivotal role in assessing corrosion fatigue intricacies. It demonstrates the significance of factors like pit dimensions, highlighting the criticality of pit depth. Moreover, the research underscores the superior predictive capabilities of machine learning, offering precise insights into the impact of corrosive environments on fatigue life. Overall, these findings emphasize the invaluable contribution of machine learning in accurately evaluating corrosion fatigue, paving the way for more robust predictive models in this domain. However, the effectiveness of data-driven methods heavily relies on the quality and availability of data, and lacking interpretability compared to physics-based models. It combines data-driven methods with physics-based models to leverage the strengths of both approaches, improving the interpretability and accuracy of predictions.

4.6. Reliability method

Fatigue failure for suspenders or cables in real-world scenarios often exhibits significant randomness and uncertainty, stemming from various sources such as load uncertainties, calculation model imprecision, and material variation. This necessitates the integration of probabilistic methods and reliability analysis into the design process. Liu et al. [95] propose a stochastic time-variant reliability assessment method for corroded steel wires, addressing the combined impact of corrosion and cyclic loading. They assume lognormal distributions

for the reduced area and its critical value to define ultimate limit states and time-variant reliability indices as:

$$Z = S_{\mathrm{c}} - S_{\mathrm{f}} \tag{72}$$

$$\beta = \frac{\mu_{\ln S_{\mathrm{c}}} - \mu_{\ln S_{\mathrm{f}}}}{\sqrt{\sigma_{\ln S_{\mathrm{c}}}^2 + \sigma_{\ln S_{\mathrm{f}}}^2}} \tag{73}$$

where S_{c} is the critical area, S_{f} is the total failure area, and β is the reliability index, and $\mu_{\ln X}$ and $\sigma_{\ln X}$ represent the mean value and standard deviation of each random variable, respectively. Fan et al. [96] present a case study of using a practical fatigue reliability-based method to form an optimal replacement schedule for stay cables, establishing the limit state function and the fatigue reliability index calculation formula:

$$Z = \ln D_{\mathrm{c}} - \ln D\left(n\right) \tag{74}$$

$$\beta = \frac{\mu_Z}{\sigma_Z} = \frac{\mu_{\ln D_c} - \ln n - m \ln S_{\mathrm{eq}} + \mu \ln C}{\sqrt{\sigma_{\ln D_{\mathrm{c}}}^2 + \sigma_{\ln C}^2}} \tag{75}$$

where D_{c} is the critical damage accumulation index and $D\left(n\right)$ is the damage accumulation parameter. Fig. 34 illustrates the reliability index variation for No. A5 and No. J21 cables considering corroded and uncorroded conditions. Their study exhibits a gradual decline in the reliability index of stay cables over service time, with the degradation less prominent in original cables compared to corroded ones. Accounting for corrosion notably reduces the reliability index, with the decline becoming more pronounced as time progressed. About the service time of 20 years, the reliability index of all corroded cables drops below a target reliability index of 3.0. This emphasizes the importance of considering corrosion in replacement schedules to ensure cables maintain adequate reliability over their service life.

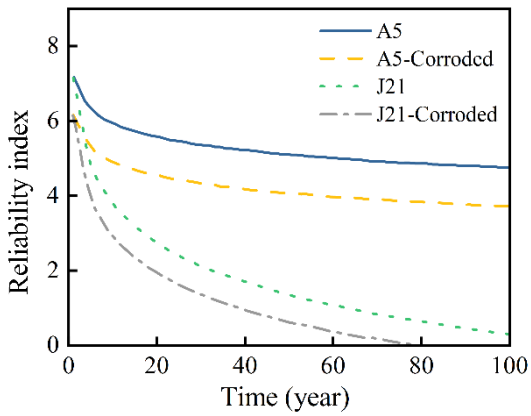

Fig. 34. Time-varying reliability indexes of original and corroded stay cables [95].

Jiang et al. [97] reveal that the combined effects of corrosion and fatigue drastically reduce the lifetime of steel wires, underscoring the insufficient fatigue resistance of stay cables under specific corrosion rates during the service life. Key parameters characterizing steel wire corrosion encompass uniform corrosion depth, maximum corrosion depth, and the decline in mechanical and fatigue properties. The uniform corrosion depth is usually computed using the exponential model:

$$d_{\mathrm{u}}(t) = C_{\mathrm{r}}\left(t - t_0\right)^{\gamma} \tag{76}$$

where t is the number of years in service, t_0 is the corrosion initiation time of the steel wire, C_{r} is the annual corrosion rate (μm/year), and γ is the long-term exponential constant. Additionally, the model defines three corrosion rate levels (low, medium, and high) for distinct environmental conditions, detailed in Table 3. The maximum pitting depth $d_{\mathrm{pmax}}(t)$ as a function of the uniform corrosion depth is expressed as:

$$d_{\mathrm{pmax}}(t) = \kappa \cdot d_{\mathrm{u}}(t) \tag{77}$$

where κ is a pitting factor that followed the Gumbel extreme distribution:

$$F(\kappa) = \exp\left[-\exp\left(-\frac{\kappa - \mu}{\beta}\right)\right] \tag{78}$$

The predicted corrosion fatigue life stands at 85 years for medium corrosion rates and drops to 24 years for high corrosion rates. The fatigue strength of the stay cable decreases accounting for the impact of corrosion. Furthermore, the cable model overestimates the

corrosion fatigue damage compared to the wire model. Highlighting the significance of the corrosion distribution among wires within the cable, it becomes imperative to factor this into the analysis of potential cable failures.

Table 3

Uniform corrosion depth parameters [97].

Corrosion rate	Steel wires inside the stay cable		
	C_r	γ	t_0
High	45	0.75	
Medium	30	0.60	1.7
Low	15	0.45	

Li et al. [98] introduced an empirical model capturing the long-term degradation of steel wire cables, accounting for uniform corrosion, pitting corrosion, and fatigue induced by cyclic loading and environmental factors. They conducted accelerated corrosion experiments to delineate various corrosion levels in high-strength steel wires and developed time-dependent statistical models to quantify both uniform and pitting corrosion depths. The corrosion-fatigue process in steel wires was simulated by integrating these corrosion models with cyclic stress derived from cable force monitoring data. Wang et al. [99] explored interlayer corrosion variance in parallel steel wire suspenders via neutral salt spray testing. They introduced a corrosion variance coefficient and delved into the stochastic degradation process of the suspenders. By integrating a daily traffic model, they developed an intricate reliability assessment method for the suspenders. Observations revealed severe corrosion in all layers of test specimens after a certain corrosion duration. Among various damage types, the annular damaged specimen displayed the most severe overall corrosion, contrasting with the vertical damaged specimen which exhibited the least. In evaluating suspenders, wire service lifespan notably varied with the corrosion variance coefficient. Fig. 35 shows the reliability indexes of different layers and the overall reliability of the suspender. Notably, the outer layer wires have a longer service lifespan compared to the inner layer wires,

positioning the overall reliability between the outer and inner layers.

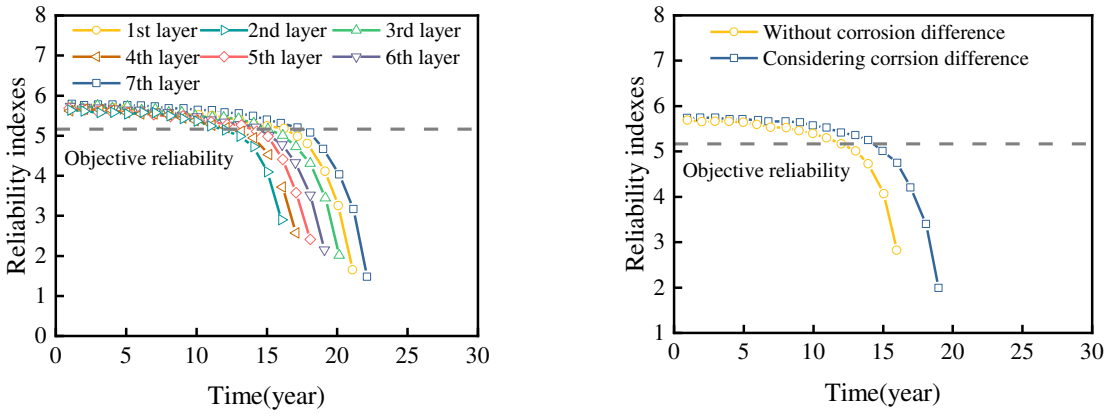

Fig. 35. (a) Reliability indexes of different layers; (b) Overall reliability indexes of the suspender [99].

To sum up, the studies delve into the unpredictability of fatigue failure in suspension cables, proposing solutions to tackle this issue. Stochastic reliability assessment methods for corroded steel wires, fatigue-based replacement scheduling for cables, and empirical models capture long-term degradation due to corrosion and cyclic loading. These approaches emphasize the vital role of considering various corrosion rates ensuring cable reliability. However, it is sensitive to input parameters and variable uncertainties, which could affect the accuracy of reliability assessments. Quantifying uncertainties associated with input parameters using probabilistic methods such as Monte Carlo simulation or Bayesian inference provides insights into the range of possible outcomes and enhances the reliability of assessments.

5. Conclusions

In this study, a detailed review of corrosion fatigue mechanisms, assessment methods, and reliability in high-strength steel wires is conducted, and the following conclusions are obtained:

(1) The corrosion fatigue process can be divided into three distinct stages: pitting formation and growth, short crack propagation, and long crack propagation. Four distinct pit morphologies have been observed, including conical pits, hemispherical pits, combined pits, and secondary pits. These corrosion pits not only introduce stress concentration but also

have a profound adverse impact on fatigue performance. Material composition, corrosive media, and external loads emerge as the main factors influencing the corrosion fatigue performance.

(2) Advanced fatigue assessment methods like the TCD and the SED are elaborated upon extensively. The fracture mechanics approach introduces a corrosion acceleration factor, designed to quantitatively assess the impact of the corrosive environment on the progression of both short and long crack growth stages. An elastoplastic corrosion fatigue damage model is employed to encapsulate the intricate mechanisms at play in scenarios involving cyclic loading and corrosive environments. Given the limitations of conventional corrosion fatigue assessment techniques, the data-driven method can accurately predict the fatigue life. It underscores the superior predictive capabilities of machine learning, offering precise insights into the impact of corrosive environments on fatigue life.

(3) Diverse models are proposed to evaluate the corrosion fatigue reliability of cables, encompassing uniform and pitting corrosion considerations. The drastic reduction in steel wire lifespans under specific corrosion rates highlights the need to consider these rates in predicting fatigue life. Additionally, the necessity of factoring corrosion distribution into analyses emphasizes its criticality in ensuring the reliability and durability of suspenders and cables in real-world scenarios, emphasizing the urgency of corrosion-aware maintenance schedules.

(4) Corrosion fatigue in high-strength steel wires is a complex process, presenting significant challenges in accurately predicting multiscale fatigue crack initiation and damage evolution. At present, a comprehensive and unified model for assessing corrosion fatigue, which accounts for the interplay of various influencing factors, is notably absent. This dearth underscores the pressing need to develop a more precise and thorough model. Future research avenues could explore both theoretical and experimental approaches to address this complexity.

CRediT authorship contribution statement

Zhiyu Jie: Investigation, Conceptualization, Methodology, Writing-Original Draft. **Zenghui Zhang:** Software, Validation. **Luca Susmel:** Methodology, Writing - Review & Editing. **Lexin Zhang:** Data curation, Formal analysis. **Wei Lu:** Visualization.

Declaration of Competing Interest

The authors declare that they have no known competing financial interests or personal relationships that could have appeared to influence the work reported in this paper.

Acknowledgements

This work is sponsored by National Natural Science Foundation of China (51708305), Zhejiang Provincial Natural Science Foundation of China (LY24E080001), China Postdoctoral Science Foundation (2023M742607), and K. C. Wong Magna Fund in Ningbo University.

References

1. Roffey P. The fracture mechanisms of main cable wires from the forth road suspension. *Eng Fail Anal*. 2013;31: 430-441.
2. Cui C, Chen A, Ma R. An improved continuum damage mechanics model for evaluating corrosion‐fatigue life of high-strength steel wires in the real service environment. *Int J Fatigue*. 2020;135: 105540.
3. Haigh BP. Experiments on the Fatigue of Brasses. *J Inst Met*. 1917;18: 55-86.
4. Mcadam JDJ. Stress-strain-cycle relationship and corrosion-fatigue of metals. *Proceedings of the ASTM*. 1926;26: 224-280.
5. Fink CG, Turner WD, Paul GT. Zinc yellow in the inhibition of corrosion fatigue of steel in sodium chloride solution. *Transactions of The Electrochemical Society*. 1943;83: 377.
6. Takeuchi M, Waterhouse RB. An investigation into the fretting-corrosion-fatigue of high strength steel wire. *Key Eng Mater*. 1988;20: 1959-1966.
7. Takeuchi M, Waterhouse RB, Mutoh Y, Satoh T. The behaviour of fatigue crack growth in the fretting‐corrosion‐fatigue of high tensile roping steel in air and seawater. *Fatigue Fract Eng M*. 1991;14: 69-77.
8. Nakamura S, Suzumura K. Experimental study on fatigue strength of corroded bridge wires. *J Bridge Eng*. 2013;18: 200-209.
9. Nakamura S, Suzumura K, Tarui T. Mechanical properties and remaining strength of corroded bridge wires. *Struct Eng Int*. 2004;14: 50-54.
10. Lan CM, Li H. Fatigue properties assessment of corroded cable. *Key Eng Mater*. 2009;413: 757-764.
11. Miao C, Yu J, Mei M. Distribution law of corrosion pits on steel suspension wires for a tied arch bridge. *Anti-Corros Method M*. 2016;63: 166-170.
12. Wan S, Zhou H, Li L, Wang C, De Filippo M, Gong F. Degradation of artificially corroded galvanized high-strength steel wires: Corrosion morphology and mechanical behavior. *Constr Build Mater*. 2022;346:

128387.
13. Li R, Miao C, Zhuang M. Experimental and numerical investigation of stress concentration factor of cable steel wire with corrosion pits. *KSCE J Civ Eng*. 2020;24: 1581-1592.
14. Guo Z, Chen H, Yao G. Bayesian prediction of the stress concentration effect on high-strength wires with corrosion pits. *Eng Fail Anal*. 2022;131: 105827.
15. Li R, Miao C, Feng Z, Wei T. Experimental study on the fatigue behavior of corroded steel wire. *J CONSTR STEEL RES*. 2021;176: 106375.
16. Ahn S, Lawrence FV, Metzger MM (1992) Corrosion fatigue of an HSLA steel. *Fatigue Fract Eng M*. 1992;15: 625-642.
17. Dolley EJ, Lee B, Wei RP. The effect of pitting corrosion on fatigue life. *Fatigue Fract Eng M*. 2000;23: 555-560.
18. Horner DA, Connolly BJ, Zhou S, Crocker L, Turnbull A. Novel images of the evolution of stress corrosion cracks from corrosion pits. *Corros Sci*. 2011;53: 3466-3485.
19. Masaki K, Ochi Y, Matsumura T. Small crack property of austenitic stainless steel with artificial corrosion pit in long life regime of fatigue. *Int J Fatigue*. 2006;28: 1603-1610.
20. Guo Z, Ma Y, Wang L, Zhang J. Modelling guidelines for corrosion-fatigue life prediction of concrete bridges: Considering corrosion pit as a notch or crack. *Eng Fail Anal*. 2019;105: 883-895.
21. Nakamura SI, Suzumura K. Hydrogen embrittlement and corrosion fatigue of corroded bridge wires. *J Constr Steel Res*. 2009;65: 269-277.
22. Liu Z, Guo T, Yu X, Huang X, Correia J. Corrosion fatigue and electrochemical behaviour of steel wires used in bridge cables. *Fatigue Fract Eng M*. 2021;44: 63-73.
23. Yao G, Yang S, Zhang J, Leng Y. Analysis of corrosion-fatigue damage and fracture mechanism of in-service bridge cables/hangers. *Adv Civ Eng*. 2021;2021: 1-10.
24. Jiang JH, Ma AB, Weng WF, et al. Corrosion fatigue performance of pre-split steel wires for high strength bridge cables. *Fatigue Fract Eng M*. 2009;32: 769-779.
25. Zhu J, Jie Z, Chen C, Zheng H, Wang W. Fatigue crack propagation of corroded high-strength steel wires using the XFEM and the EIFS. *Materials*. 2023;16: 4738-4752.
26. Chen C, Jie Z, Wang K. Fatigue life evaluation of high-strength steel wires with multiple corrosion pits based on the TCD. *J Constr Steel Res*. 2021;186: 106913.
27. Jie Z, Susmel L. High-strength steel wires containing corrosion pits: stress analysis and critical distance based fatigue life estimation. *Fatigue Fract Eng M*. 2020;43: 1611-1629.
28. Li CX, Tang XS, Xiang GB. Fatigue crack growth of cable steel wires in a suspension bridge: Multiscaling and mesoscopic fracture mechanics. *Theor Appl Fract Mec*. 2010;53: 113-126.
29. Jie Z, Berto F, Susmel L. Fatigue behaviour of pitted/cracked high-strength steel wires based on the SED approach. *Int J Fatigue*. 2020;135: 105564.
30. Ye H, Duan Z, Tang S, Yang Z, Xu X. Fatigue crack growth and interaction of bridge wire with multiple surface cracks. *ENG FAIL ANAL*.2020;116: 104739.
31. Wang G, Ma Y, Wang L, Zhang J. Experimental study and residual fatigue life assessment of corroded high-tensile steel wires using 3D scanning technology. *Eng Fail Anal*. 2021;124: 105335.
32. Sun B. A continuum model for damage evolution simulation of the high strength bridge wires due to corrosion fatigue. *J Constr Steel Res*. 2018;146: 76-83.

33. Fan C, Li Z, Wang Y. A multi-scale corrosion fatigue damage model of high-strength bridge wires. *Int J Damage Mech*. 2020;29: 887-901.
34. Lu Q, Zhu J, Zhang W. Quantification of fatigue damage for structural details in slender coastal bridges using machine learning-based methods. *J Bridge Eng*. 2020;25: 4020033.
35. Yan F, Song K, Liu Y, Chen S, Chen J. Predictions and mechanism analyses of the fatigue strength of steel based on machine learning. *J MATER SCI*. 2020;55: 15334-15349.
36. Kamble RG, Raykar NR, Jadhav DN. Machine learning approach to predict fatigue crack growth. *Mater Today: Proc*. 2021;38: 2506-2511.
37. Deng Y, Li AQ, Feng DM, Chen X, Zhang M. Service life prediction for steel wires in hangers of a newly built suspension bridge considering corrosion fatigue and traffic growth. *Struct Control Hlth*. 2020;27: e2642.
38. Bai N, Li H, Ma J, Lan C, Spencer Jr BF. Fatigue life evaluation model for high-strength steel wire considering different levels of corrosion. *Struct Infrastruct E*. 2022;19: 409-419.
39. Lan C, Xu Y, Liu C, Li H, Spencer Jr BF. Fatigue life prediction for parallel-wire stay cables considering corrosion effects. *Int J Fatigue*. 2018;114: 81-91.
40. Song Y, Ding Y, Zhong W, Zhao H. Reliable fatigue-life assessment of short steel hanger in a rigid tied arch bridge integrating multiple factors. *J Perform Constr Fac*. 2018;32: 4018038.
41. Zhang H, Yao L, Zheng X, Shen M, Xie X. Corrosion-fatigue analysis of wires in bridge cables considering time-dependent electrochemical corrosion process. *J Eng Mech*. 2023;149: 4023019.
42. Mayrbaurl RM, Camo S. guidelines for inspection and strength evaluation of suspension bridge parallel-wire cables. NCHRP Report 534.2004
43. Nakamura S, Suzumura K. Experimental study on fatigue strength of corroded bridge wires. *J Bridge Eng*. 2013;18: 200-209.
44. Miyachi K, Chryssanthopoulos M, Nakamura S. Experimental assessment of the fatigue strength of corroded bridge wires using non-contact mapping techniques. *Corros Sci*. 2021;178: 109047.
45. Cerit M, Genel K, Eksi S. Numerical investigation on stress concentration of corrosion pit. *Eng Fail Anal*. 2009;16: 2467-2472.
46. Wang G, Ma Y, Wang L, Su X, Zhang J. Numerical investigation of stress concentration factor induced by multiple scenarios of adjacent corrosion pits. *Structures*. 2020; 26:572-581.
47. Li R, Miao C, Yu J. Effect of characteristic parameters of pitting on strength and stress concentration factor of cable steel wire. *Constr Build Mater*. 2020;240: 117915.
48. Wang R. *Corrosion fatigue of metallic materials*. Northwestern Polytechnical University Press, Xi'an, China; 2001
49. Zhao W, Xin R, He Z, Wang Y. Contribution of anodic dissolution to the corrosion fatigue crack propagation of X80 steel in 3.5wt.% NaCl solution. *Corros Sci*. 2012;63: 387-392.
50. Chen J, Diao B, He J, Pang S, Guan X. Equivalent surface defect model for fatigue life prediction of steel reinforcing bars with pitting corrosion. *Int J FatiguE*. 2018;110: 153-161.
51. Jie ZY. Study on the fatigue performance of welded joints in steel bridges under prior corrosion and complex stress fields. Southwest Jiaotong University, Chengdu, China;2015.
52. Wei L. Projected area approach for pitting corrosion fatigue life prediction. Nanjing University of Aeronautics and Astronautics, Nanjing, China;2008
53. Wei RP. Some aspects of environment-enhanced fatigue-crack growth. *Eng Fract Mech*. 1970;1: 633-651.

54. Austen IM, McIntyre P. Corrosion fatigue of high-strength steel in low-pressure hydrogen gas. *Met Sci*. 1979;13: 420-428.
55. Yuan Y, Liu X, Pu G, Wang T, Guo Q. Corrosion features and time-dependent corrosion model of Galfan coating of high strength steel wires. *Constr Build Mater*. 2021;313: 125534.
56. Zhao Y, Su B, Fan X, Yuan Y, Zhu Y. Corrosion fatigue degradation characteristics of galvanized and galfan high-strength steel wire. *Materials*. 2023;16: 708-720.
57. Zhang Z, Wang L, Song S, et al. Effect of coating on stress corrosion performance of bridge cable steel wire. *Coatings*. 2023;13: 1339-1357.
58. Suzumura K, Nakamura S. Environmental factors affecting corrosion of galvanized steel wires. *J Mater Civil Eng*. 2004;16: 1-7.
59. Wu S, Chen H, Ramandi HL, Hagan PC, Crosky A, Saydam S. Effects of environmental factors on stress corrosion cracking of cold-drawn high-carbon steel wires. *Corros Sci*. 2018;132: 234-243.
60. Wang Y, Zhang W, Zheng Y. Experimental study on corrosion fatigue performance of high-strength steel wire with initial defect for bridge cable. *Appl Sci-basel*. 2020;10: 2293.
61. Miao CQ, Zhuang ML, Dong B. Stress corrosion of bridge cable wire by the response surface method. *Strength Mater+*. 2019;51: 646-652.
62. Wang SQ, Zhang DK, Hu NN, Zhang JL. Effect of Stress Ratio and Loading Frequency on the Corrosion Fatigue Behavior of Smooth Steel Wire in Different Solutions. *Materials*. 2016;9: 750-756.
63. Zhang L, Liang Z, Li S. Effect of current density on the cathodic protection efficiency and mechanical properties of pre-stressed high-strength steel wires for stay cable. *Constr Build Mater*. 2022;314: 125671.
64. Jie Z, Chen C, Berto F, Wang K, Peng X. Effect of stress ratios on corrosion fatigue life of high-strength steel wires. *Fatigue Fract Eng M*. 2022;45: 593-606.
65. Yao G, Yu X, Gu L, Jiang Y. Experiment on corrosion fatigue life of steel strands under the coupling effects of chloride environment and alternating loads. *Adv Civ Eng*. 2021;2021: 1-12.
66. Yu X. Study on the durability of steel wire under the coupling effects of harsh environment and variable loads. *Eng Fail Anal*.2024;157: 107487.
67. GB/T 10125. Corrosion tests in artificial atmospheres-Salt spray tests. Standards Press of China;2012.
68. Ma Y, He Y, Wang G, Wang L, Zhang J, Lee D. Corrosion fatigue crack growth prediction of bridge suspender wires using Bayesian gaussian process. *Int J Fatigue*. 2023;168: 107377.
69. Guo Z, Ma Y, Wang L, Zhang J, Harik IE. Corrosion fatigue crack propagation mechanism of high-strength steel bar in various environments. *J Mater Civil Eng*. 2020;32: 4020115.
70. ASTM E647. Standard test method for measurement of fatigue crack growth rates;2013.
71. Peng W, Fan W. Experimental study on corrosion development model and fatigue performance of strand steel for coastal structures. *J Mar Sci Eng*. 2023;11: 665-677.
72. Xue S, Shen R, Chen W, Shen L. The corrosion-fatigue measurement test of the Zn-Al alloy coated steel wire. *Structures*. 2020;27: 1195-1201.
73. Deng Y, Deng L. Corrosion fatigue test and performance evaluation of high-strength steel wires based on the suspender of a 11-year-old concrete-filled steel tube arch bridge. *Coatings*. 2022;12: 1475.
74. Miao C, Li R, Yu J. Effects of characteristic parameters of corrosion pits on the fatigue life of the steel wires. *J Constr Steel Res*. 2020;168: 105879.
75. Susmel L, Taylor D. A novel formulation of the theory of critical distances to estimate lifetime of notched

components in the medium-cycle fatigue regime. *Fatigue Fract Eng M*. 32007;0: 567-581.
76. Lazzarin P, Berto F, Gomez FJ, Zappalorto M. Some advantages derived from the use of the strain energy density over a control volume in fatigue strength assessments of welded joints. *Int J Fatigue*. 2008;30: 1345-1357.
77. Lazzarin P, Zambardi R. A finite-volume-energy based approach to predict the static and fatigue behavior of components with sharp V-shaped notches. *Int J Fracture*. 2001;112: 275-298.
78. Mao M, Zhang X, Tu S, Xuan F. Prediction of crack initiation life due to corrosion pits. *J Aircraft*. 2014;51: 805-810.
79. Sih GC, Tang XS, Mahmoud KM, Kassir MK. Effect of crack shape and size on estimating the fracture strength and crack growth fatigue life of bridge cable steel wires. *Bridge Struct*. 2008;4: 3-13.
80. Jiang C, Wu C, Jiang X. Experimental study on fatigue performance of corroded high-strength steel wires used in bridges. *Constr Build Mater*. 2018;187: 681-690.
81. Zheng H, Jie Z, Zhang L, Lu W. Fatigue crack growth and life assessment of full penetration U-rib welded joints considering residual stresses. *Thin Wall Struct*. 2024;195: 111426.
82. Jie Z, Li Y, Wei X. A study of fatigue crack growth from artificial corrosion pits at welded joints under complex stress fields. *Fatigue Fract Eng M*. 2017;40: 1364-1377.
83. Martín A, Sánchez-Gálvez V. Environmentally assisted fatigue crack growth in high strength eutectoid cold drawn steel. *Brit Corros J*. 1988;23: 96-101.
84. Xue S, Shen R. Corrosion-fatigue analysis of high-strength steel wire by experiment and the numerical simulation. *Metals-basel*.2020; 10: 734-745.
85. Wang Y, Zheng YQ, Zhang WH, Lu QR. Analysis on damage evolution and corrosion fatigue performance of high-strength steel wire for bridge cable: Experiments and numerical simulation. *Theor Appl Fract Mec*. 2020;107: 102571.
86. Zheng Y, Wang Y. Damage evolution simulation and life prediction of high-strength steel wire under the coupling of corrosion and fatigue. *Corros Sci*. 2020;164: 108368.
87. Cheng Y, Huang WL, Zhou CY. Artificial neural network technology for the data processing of on-line corrosion fatigue crack growth monitoring. *Int J Pres Ves Pip*. 1999;76: 113-116.
88. Wang H, Zhang W, Sun F, Zhang W. A comparison study of machine learning based algorithms for fatigue crack growth calculation. *Materials*. 2017;10: 543.
89. Feng C, Su M, Xu L, Zhao L, Han Y. Estimation of fatigue life of welded structures incorporating importance analysis of influence factors: A data-driven approach. *Eng Fract Mech*. 2023: 281:109103.
90. Dourado A, Viana FA. Physics-informed neural networks for missing physics estimation in cumulative damage models: a case study in corrosion fatigue. *J Comput Inf Sci Eng*. 2020;20: 61007.
91. Feng C, Su M, Xu L, Zhao L, Han Y, Peng C. A novel generalization ability-enhanced approach for corrosion fatigue life prediction of marine welded structures. *Int J Fatigue*. 2023;166: 107222.
92. Yu X, Zhang G, Jin H, Song X. A data driven model for estimating the fatigue life of 7075-T651 aluminum alloy based on the updated BP model. *J Mater Res Technol*. 2023;24: 1252-1263.
93. Feng C, Su M, Xu L, Zhao L, Han Y, Peng C. A novel generalization ability-enhanced approach for corrosion fatigue life prediction of marine welded structures. *Int J Fatigue*. 2023;166: 107222.
94. Guo X, Liu X, Long G, Zhao Y, Yuan Y. Data-driven prediction of the fatigue performance of corroded high-strength steel wires. *Eng Fail Anal*. 2023;146: 107108.

95. Liu Z, Guo T, Hebdon MH, Zhang Z. Corrosion fatigue analysis and reliability assessment of short suspenders in suspension and arch bridges. *J Perform Constr Fac*. 2018;32: 4018060.
96. Fan Z, Ye Q, Xu X, Ren Y, Huang Q, Li W. Fatigue reliability-based replacement strategy for bridge stay cables: A case study in China. *Structures*. 2022;39: 1176-1188.
97. Jiang C, Wu C, Cai CS, Jiang X, Xiong W. Corrosion fatigue analysis of stay cables under combined loads of random traffic and wind. *Eng Struct*. 2020;206: 110153.
98. Li S, Xu Y, Zhu S, Guan X, Bao Y. Probabilistic deterioration model of high-strength steel wires and its application to bridge cables. *Struct Infrastruct E*. 2015;11: 1240-1249.
99. Wang D, Zhao Y, Guo X, Yuan Y, Li X. Reliability assessment of parallel wire suspender components considering interlayer corrosion variance. *Structures*. 2023;47: 81-92.